RESEARCH ARTICLE

Deployment of endocytic machinery to periactive zones of nerve terminals is independent of active zone assembly and evoked release

Javier Emperador-Melero[1,2†], Steven J Del Signore[3†], Kevin M De León González[3], Pascal S Kaeser[1*‡], Avital A Rodal[3*‡]

[1]Department of Neurobiology, Harvard Medical School, Boston, United States; [2]Department of Neuroscience and Institute for Translational Neuroscience, New York University Grossman School of Medicine, New York, United States; [3]Department of Biology, Brandeis University, Waltham, United States

***For correspondence:** kaeser@hms.harvard.edu (PSK); arodal@brandeis.edu (AAR)

[†]These authors contributed equally to this work
[‡]These authors also contributed equally to this work

Competing interest: The authors declare that no competing interests exist.

Funding: See page 28

Preprint posted
27 April 2025
Sent for Review
23 April 2025
Reviewed preprint posted
23 June 2025
Reviewed preprint revised
18 May 2026
Version of Record
17 June 2026

Reviewing Editor: Dion K Dickman, University of Southern California, United States

© Copyright Emperador-Melero, Del Signore *et al*. This article is distributed under the terms of the Creative Commons Attribution License, which permits unrestricted use and redistribution provided that the original author and source are credited.

eLife Assessment

This is an **important** and rigorous study that addresses the question of what determines the spatial organization of endocytic zones at synapses. The authors use **compelling** approaches, in both *Drosophila* and rodent model systems, to define the role of activity and active zone structure on the organization of the periactive zone. While the findings are primarily negative, they are carefully executed and contribute to the field by refining existing models of presynaptic organization.

Abstract In presynaptic nerve terminals, the endocytic apparatus rapidly restores synaptic vesicles after neurotransmitter release. Many endocytic proteins localize to the periactive zone, a loosely defined area adjacent to active zones. A prevailing model posits that recruitment of these endocytic proteins to the periactive zone is activity-dependent. We show that periactive zone targeting of endocytic proteins is largely independent of active zone machinery and synaptic activity. At mouse hippocampal synapses and *Drosophila* neuromuscular junctions, pharmacological or genetic silencing resulted in unchanged or increased levels of endocytic proteins including Dynamin, Amphiphysin, Nervous Wreck, Endophilin A, Dap160/Intersectin, PIPK1γ, and AP-180. Similarly, disruption of active zone assembly via genetic ablation of active zone scaffolds at each synapse did not impair the localization of endocytic proteins. Overall, our work indicates that endocytic proteins are constitutively deployed to the periactive zone and supports the existence of independent assembly pathways for active zones and periactive zones.

Introduction

Release of neurotransmitters relies on the coordinated function of two complementary protein machineries, each comprising many proteins. First, the active zone defines vesicular release sites and clusters voltage-gated Ca^{2+} channels of the Ca_V2 family for rapid fusion of synaptic vesicles in response to action potentials (***Emperador-Melero and Kaeser, 2020***; ***Südhof, 2012***). Second, the endocytic apparatus restores vesicles after exocytosis for subsequent rounds of refilling and release. The endocytic machinery is enriched at the periactive zone, a region typically localized adjacent to the active zone (***Haucke et al., 2011***; ***Saheki and De Camilli, 2012***; ***Watanabe and Boucrot, 2017***). Despite the functional relationships between exocytosis and endocytosis and the spatial coupling of

their respective protein machineries, the mechanisms that determine the recruitment of the endocytic apparatus to the periactive zone remain uncertain.

One model posits that deployment of endocytic machinery to the periactive zone occurs in response to synaptic activity. Multiple lines of evidence support this model. First, depolarization causes some endocytic proteins (including Dap160/Intersectin, Endophilin, and Dynamin) to partially relocalize from the vesicle pool to the cytosol or plasma membrane (***Bai et al., 2010***; ***Jiang et al., 2024***; ***Koh et al., 2007***; ***Winther et al., 2015***; ***Winther et al., 2013***). Second, membrane uptake increases rapidly in response to exocytosis triggered by synaptic activity (***Haucke et al., 2011***; ***Saheki and De Camilli, 2012***; ***Watanabe and Boucrot, 2017***), indicating that the endocytic protein machinery is responsive to activity and might be recruited to the membrane in consequence. Third, activity-dependent mechanisms at synapses might parallel protein deployment for Clathrin-mediated endocytosis in non-neuronal cells, where cytosolic endocytic machinery is transiently and acutely recruited to discrete sites (***Cocucci et al., 2014***; ***Kaksonen and Roux, 2018***; ***Taylor et al., 2011***). Fourth, the distributions of Clathrin, the Clathrin adaptor γ-Adaptin, and one Dynamin isoform become diffuse after blocking action potentials in neurons with impaired endocytosis (***Ferguson et al., 2007***; ***Milosevic et al., 2011***; ***Raimondi et al., 2011***).

An alternative model in which the endocytic apparatus is constitutively recruited to the periactive zone is also supported by previous work. For example, unstimulated synapses contain endocytic machinery at the periactive zone (***Bloom et al., 2003***; ***Del Signore et al., 2023***; ***Estes et al., 1996***; ***Gerth et al., 2017***; ***Imoto et al., 2022***; ***Roos and Kelly, 1999***; ***Wahl et al., 2013***; ***Winther et al., 2015***; ***Winther et al., 2013***), raising the possibility that periactive zone assembly relies on active zone proteins or other activity-independent mechanisms. Furthermore, ultrafast endocytosis requires pre-deployment of Dynamin and pre-assembly of a ring of F-actin surrounding the active zone (***Watanabe et al., 2013***; ***Imoto et al., 2022***; ***Ogunmowo et al., 2023***). In addition, endocytic machinery is required to prevent rapid synaptic depression, which occurs at a timescale that might exceed the speed of activity-dependent protein recruitment (***Hua et al., 2011***; ***Jäpel et al., 2020***; ***Kawasaki et al., 2000***). Moreover, the endocytic machinery is involved in functions that span beyond endocytosis and are more likely to depend on predeployment of machinery to the plasma membrane. These include the regulation of the exocytic fusion pore, the fusion of dense core vesicles, and the trafficking of adhesion molecules, growth factors, and extracellular vesicle cargoes (***Anantharam et al., 2011***; ***Bailey et al., 1992***; ***Blanchette et al., 2022***; ***Fu and Huang, 2010***; ***Moro et al., 2021***; ***Rodal et al., 2008***; ***Samasilp et al., 2012***). Overall, it has remained uncertain whether endocytic machinery is predeployed or recruited on an as-needed basis by activity.

Here, we combine genetic and pharmacological manipulations at two model synapses to test whether the recruitment of endocytic machinery to the periactive zone depends on synaptic activity or active zone scaffolds. Our work establishes that endocytic machinery is efficiently targeted to synapses and deployed to the periactive zone when evoked synaptic activity is chronically inhibited either pharmacologically or genetically. Furthermore, multiple active zone organizers, including RIM, ELKS, and its homolog Brp, Liprin-α, and Rab3 were not required for recruitment and positioning of endocytic proteins to the periactive zone. Our findings support that endocytic machinery is constitutively deployed to presynaptic nerve terminals and localizes to periactive zones independent of active zone assembly and evoked synaptic vesicle release.

Results

Localization of endocytic proteins after silencing or depolarization of mouse hippocampal neurons

We generated primary neurons from mouse hippocampi and modulated their activity either by silencing them chronically or by triggering exocytosis acutely (***Figure 1A***). We then assessed the distribution of endocytic proteins in these conditions compared to untreated neurons. To chronically inhibit activity, we simultaneously blocked action potentials with the Na^+ channel blocker tetrodotoxin (TTX) and Ca^{2+} entry with blockers of $Ca_V2.1$ (ω-agatoxin IVA; ω-Aga) and $Ca_V2.2$ (ω-conotoxin GVIA; ω-Cono) channels. We added this drug cocktail at 3 days in vitro (DIV) and resupplied it every 3 days, which results in continuous inhibition, as established before (***Held et al., 2020***). To acutely trigger exocytosis in neurons that were not treated with blockers, we depolarized neurons with superfusion of

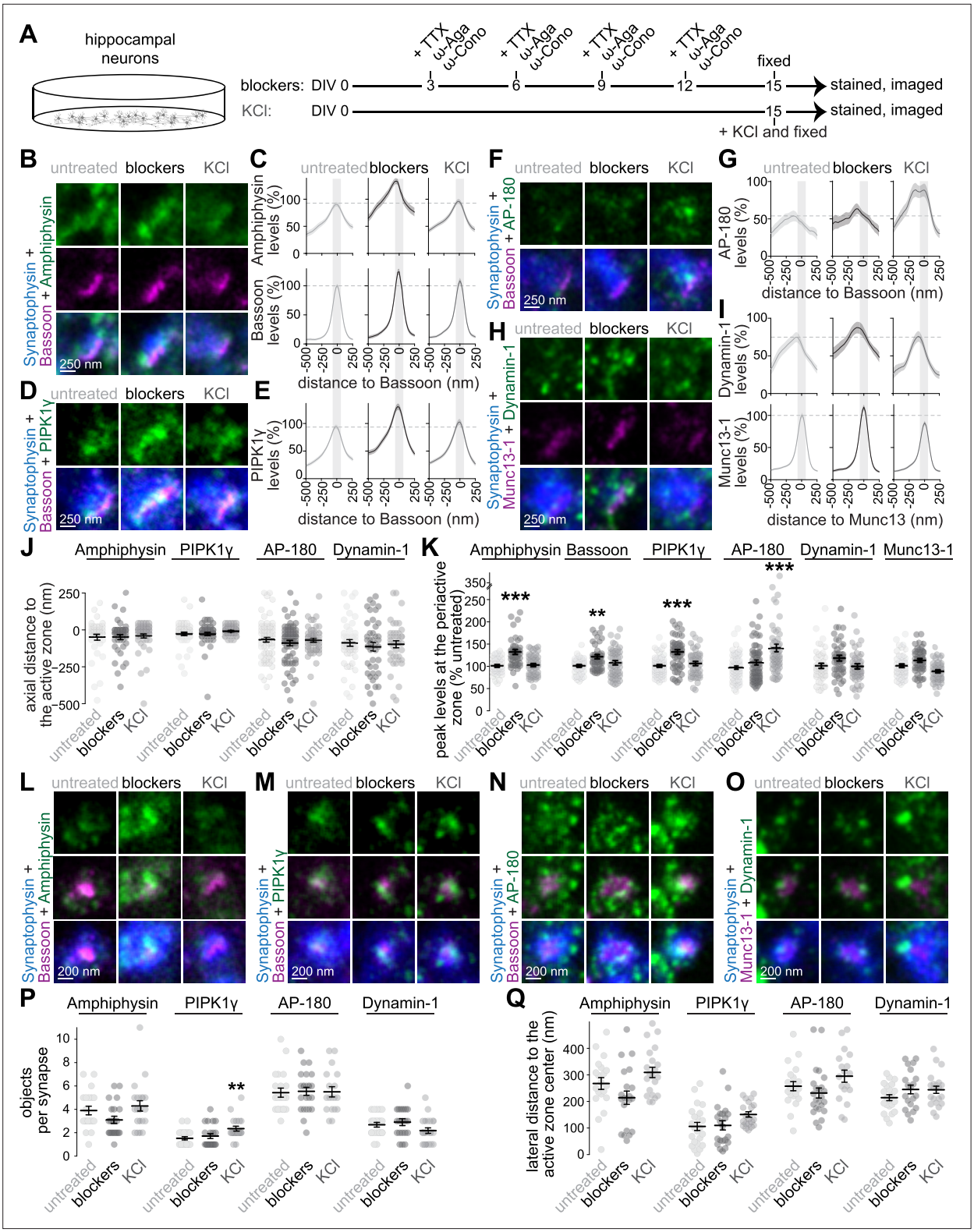

Figure 1. Deployment of endocytic proteins after chronic silencing or acute depolarization of mouse hippocampal neurons. (**A**) Schematic of the experiment in mouse hippocampal neurons. For chronic silencing, a cocktail ('blockers') with tetrodotoxin (TTX, 1 μM final concentration), ω-agatoxin IVA (ω-Aga, 250 nM), and ω-conotoxin GVIA (ω-Cono, 200 nM) was added every 3 days starting DIV3. For acute depolarization ('KCl'), neurons were stimulated with 50 mM KCl for 30 s before fixation. (**B–I**) Example side-view synapses and average line profiles for neurons stained for Bassoon, Synaptophysin, and Amphiphysin (B, C), PIPK1γ (D, E), or AP-180 (F, G), or Synaptophysin, Munc13-1, and Dynamin-1 (H, I). Neurons were stained for

Figure 1 continued on next page

Figure 1 continued

a protein of interest (Amphiphysin, PIPK1γ, AP-180, or Dynamin-1; imaged in STED), an active zone marker (Bassoon or Munc13-1; imaged in STED), and Synaptophysin (imaged in confocal). An area of interest was positioned perpendicular to the center of the active zone marker, and synapses were aligned via the peak fluorescence of the active zone marker in the average profiles (**C, E, G, I**). Line profile plots were normalized to the average signal in the untreated condition. Dashed lines in C, E, G, and I mark average levels in the untreated condition, and gray shaded areas represent the active zone and periactive zone area; n in B, C (synapses/cultures): untreated 38/3, blockers 40/3, KCl 45/3; D, E: untreated 51/3, blockers 49/3, KCl 42/3; F, G: untreated 58/3, blockers 61/3, KCl 50/3; H, I: untreated 45/3, blockers 43/3, KCl 42/3. (**J, K**) Quantification and statistical analyses of the experiment shown in B–I, including peak-to-peak distance of the active zone marker and the protein of interest (**J**), and of the peak levels in the periactive zone area (**K**). The periactive zone area is defined as an area within 68 nm on each side of the peak of the active zone marker (gray shaded areas in **C, E, G, I**); n as in B–I. (**L–Q**) Example en-face synapses (**L–O**) and quantification of the number of objects (**P**) and distance of these objects to the center of the active zone marker (**Q**) of the experiment shown in A–K; n in P, Q (synapses/cultures): Amphiphysin, untreated 20/3, blockers 21/3, KCl 21/3; PIPK1γ, untreated 23/3, blockers 21/3, KCl 20/3; AP-180, untreated 21/3, blockers 24/3, KCl 18/3; Dynamin-1, untreated 22/3, blockers 20/3, KCl 22/3. Data are shown as mean ± SEM; *p < 0.05, **p < 0.05, ***p < 0.001 shown compared to the untreated condition determined by Kruskal–Wallis followed by Holm post hoc tests (J for Amphiphysin, PIPK1γ, and AP-180; K, P, Q), or by one-way ANOVA followed by a Tukey–Kramer post hoc test (J for Dynamin-1). For quantification of confocal images, see ***Figure 1—figure supplement 1***; for a workflow of STED analyses, see ***Figure 1—figure supplement 2***; for assessment of AP-180 using an independent antibody, see ***Figure 1—figure supplement 3***, for additional analyses of en-face synapses, see ***Figure 1—figure supplement 4***.

The online version of this article includes the following figure supplement(s) for figure 1:

Figure supplement 1. Confocal microscopic analyses of synapses after chronic silencing or acute depolarization of mouse hippocampal neurons.

Figure supplement 2. Workflows for STED analyses in mouse hippocampal neurons and for confocal analyses at *Drosophila* neuromuscular junctions.

Figure supplement 3. Assessment of AP-180 with alternate antibody after chronic silencing or acute depolarization of mouse hippocampal neurons.

Figure supplement 4. Additional analyses of en-face synapses after chronic silencing or acute depolarization of mouse hippocampal neurons.

50 mM KCl for 30 s. These two paradigms were used to test whether synaptic transmission contributes to the assembly of the periactive zone.

We fixed the neurons that were either treated with blockers (for at least 12 days) or depolarized acutely and used antibody staining to label components of the synaptic endocytic machinery. This machinery contains multiple proteins that belong to several categories including (1) BAR-domain containing proteins that sense and generate membrane invaginations, (2) phosphoinositide enzymes that regulate lipid metabolism, (3) components of Clathrin coats that sort recycled proteins, and (4) Dynamin proteins that operate in membrane fission. We labeled the BAR-domain containing protein Amphiphysin, the phosphoinositide kinase PIPK1γ, the Clathrin adaptor AP-180, and Dynamin-1 (***Di Paolo et al., 2002***; ***Koo et al., 2015***; ***Raimondi et al., 2011***; ***Wenk et al., 2001***). We co-stained for the synaptic vesicle marker Synaptophysin, and an active zone marker (either the scaffold Bassoon or the vesicle priming protein Munc13-1, as we did before ***Wong et al., 2018***). We detected signals generated by these antibodies using two complementary approaches as we described before (***Emperador-Melero et al., 2024***; ***Emperador-Melero et al., 2021b***): confocal microscopy was used to quantify protein levels in presynaptic boutons, and stimulated emission depletion (STED) microscopy was employed to assess subsynaptic protein distributions and levels at the presynaptic plasma membrane.

To estimate synaptic levels in confocal images, we quantified the average signal intensities of the proteins within regions of interest defined by Synaptophysin staining using a thresholding and segmentation method established before (***Emperador-Melero et al., 2024***; ***Emperador-Melero et al., 2021b***; ***Liu et al., 2018***). The average Amphiphysin, PIPK1γ, and AP-180 signal intensities were increased by up to 40% after chronic inhibition of activity, and those of Dynamin-1 were unaffected (***Figure 1—figure supplement 1A, B***). Enhanced levels in this condition were also present for the vesicle protein Synaptophysin and for Munc13-1 and may reflect a homeostatic increase of presynaptic material in response to chronic silencing. Hence, blocking action potentials and Ca^{2+} entry did not decrease the targeting of endocytic proteins to synapses. Acute depolarization enhanced the signal intensity of AP-180 by ~30%, while Amphiphysin, PIPK1γ, and Dynamin-1 were not increased. The increase in AP-180 may reflect that some endocytic proteins can be further recruited to synapses in response to strong depolarization, matching previous reports (***Bolz et al., 2023***; ***Mueller et al., 2004***).

To assess subsynaptic protein localizations, we analyzed side-view and en-face synapses after acquiring images with STED microscopy (***Figure 1—figure supplement 2A***). Side-view analyses enable the assessment of protein distributions axially from the plasma membrane to the inside of the

bouton. We identified side-view synapses as those containing an elongated area of an active zone marker (Bassoon or Munc13) at the edge of a Synaptophysin cloud. We then extracted the distribution of the protein of interest by positioning a line profile perpendicular to the active zone marker, as we did before (***Chin and Kaeser, 2024***; ***Emperador-Melero et al., 2024***; ***Emperador-Melero et al., 2021b***; ***Held et al., 2020***; ***Tan et al., 2022***). At untreated synapses, the distributions of Amphiphysin, PIPK1γ, AP-180, and Dynamin-1 were broader than those of active zone proteins (***Figure 1B–I***), consistent with localization at the periactive zone and in the presynaptic cytosol (***Ganguly et al., 2021***; ***Gerth et al., 2017***; ***Wenk et al., 2001***). The average peak signal intensities of these proteins were within ~100 nm of the peak of the active zone marker (***Figure 1J***). To estimate levels at the presynaptic plasma membrane, we measured the signal intensities within a 135-nm region centered around the peak of the active zone marker (***Wong et al., 2018***), which likely includes the active zone and the periactive zone because the two regions overlap in side-view. The signal intensities for Amphiphysin and PIPK1γ in this region were increased upon chronic silencing, matching the higher synaptic levels quantified in confocal images, and the intensities of AP-180 and Dynamin-1 were similar to the untreated condition (***Figure 1K***). The levels of AP-180, but not of the other three proteins, increased with KCl depolarization (***Figure 1K***), matching the confocal data (***Figure 1—figure supplement 1A, B***). We observed a similar increase in AP-180 signals using an alternate antibody (***Figure 1—figure supplement 3***). We did not detect changes in the axial distribution of any of these proteins (***Figure 1J***). Overall, these observations suggest that the localization of endocytic proteins to the presynaptic plasma membrane does not require action potential firing and presynaptic Ca^{2+} entry but instead indicate activity-independent recruitment.

Next, we analyzed en-face synapses to assess the lateral protein distribution near the plane of the plasma membrane (***Figure 1—figure supplement 2B***). We identified en-face synapses as those that did not have a bar-like appearance of the marker; instead, the area of the marker was surrounded by Synaptophysin staining (***Emperador-Melero et al., 2024***). At untreated synapses, Amphiphysin, AP-180, and Dynamin were organized into multiple clusters adjacent to the active zone. On average, these clusters were located 200–300 nm lateral from the center of the active zone marker (***Figure 1L–Q***). The average distribution of PIPK1γ appeared closer to the active zone, possibly reflecting its roles in the synthesis of phosphatidylinositol 4,5-bisphosphate ($PI(4,5)P_2$), a phospholipid important for both exo- and endocytosis (***Bai et al., 2004***; ***Bolz et al., 2023***; ***Di Paolo et al., 2004***; ***Wenk et al., 2001***). Neither chronic silencing nor strong depolarization changed the lateral distribution of these proteins. Instead, they remained distributed in clusters surrounding the active zone (***Figure 1L–Q***). There was a slight increase in the number of PIPK1γ objects upon depolarization (***Figure 1P***). Upon chronic silencing, the integrated intensity of endocytic protein clusters (defined as the product of their size and average intensity) increased or showed a positive trend for all proteins (***Figure 1—figure supplement 4***). The integrated intensity also increased for AP-180 upon depolarization, matching with the higher levels measured at side-view synapses and at confocal resolution (***Figure 1***, ***Figure 1—figure supplement 4***).

Together, these experiments indicate that while endocytic proteins are not impervious to synaptic activity, they are efficiently deployed to presynaptic terminals and to the periactive zone after pharmacological silencing of firing activity and Ca^{2+} entry.

Localization of endocytic proteins after chronic silencing or acute stimulation of *Drosophila* NMJs

We next asked whether recruitment of endocytic proteins to the presynaptic plasma membrane follows a similar pattern at the *Drosophila* neuromuscular junction (NMJ). This is a widely used model to study synaptic architecture that contains well-defined periactive zones (***Harris and Littleton, 2015***). First, we used antibody labeling and STED microscopy to characterize the degree to which the endocytic proteins Dynamin, Endophilin-A (EndoA), and Dap160 (the homolog of the mammalian Intersectin) localize to the synaptic vesicle cloud or periactive zone (***Figure 2***, ***Figure 2—figure supplement 1***). To do so, we measured their co-localization with the endocytic protein Nervous Wreck (FCHSD2 homolog), which exhibits strongly polarized localization to the periactive zone (***Del Signore et al., 2023***), or with the vesicle pool marker Synapsin. In all cases, the co-localization of these proteins with Nervous Wreck or Synapsin was partial, supporting broad distributions spanning the periactive zone and the vesicle cloud, and aligning with the distributions of endocytic proteins in mouse hippocampal

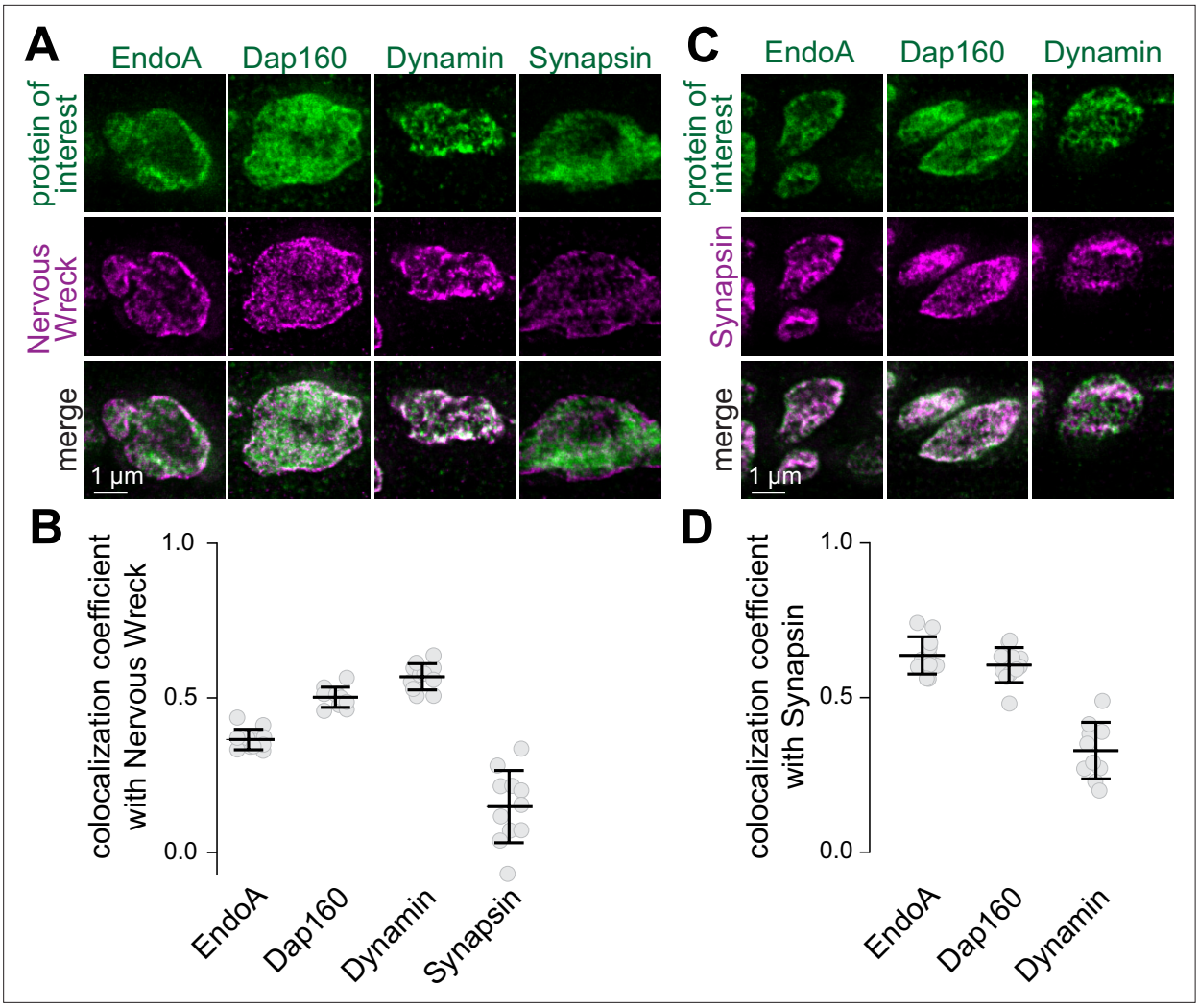

Figure 2. Localization of endocytic proteins at *Drosophila* NMJs relative to Synapsin or Nervous Wreck. (**A, B**) Example boutons of *Drosophila* NMJs stained for Nervous Wreck and either EndoA, Dap160, Dynamin, or Synapsin, and quantification of the co-localization between Nervous Wreck and these proteins measured as the Pearson's coefficient; n (NMJ/animals): EndoA 11/3, Dap160 10/3, Dynamin 11/3, Synapsin 11/3. (**C, D**) Same as A, B but relative to Synapsin instead of Nervous Wreck; n (NMJ/animals): EndoA 11/3, Dap160 11/3, Dynamin 10/3. Data are shown as mean ± SEM. Images acquired by STED microscopy. For antibody validation, see ***Figure 2—figure supplement 1***.

The online version of this article includes the following figure supplement(s) for figure 2:

Figure supplement 1. Validation of EndoA, Dap160, and Dynamin antibodies in *Drosophila* NMJs.

neurons (***Figure 1***) and with previous reports (***Bai et al., 2010***; ***Ganguly et al., 2021***; ***Gerth et al., 2017***; ***Wenk et al., 2001***).

Next, we assessed whether the distribution of endocytic proteins is changed by synaptic activity. We silenced Type 1b motor neurons on muscle 1 by expressing Tetanus Neurotoxin (TeNT). We employed a single-neuron driver (***Jenett et al., 2012***), as silencing NMJs broadly is lethal (***Sweeney et al., 1995***), and used motor neurons expressing the GAL4 driver alone as controls (***Figure 3A***). We then used antibody staining against the active zone marker Bruchpilot (Brp), which is the homolog of ELKS (***Kittel et al., 2006***; ***Wagh et al., 2006***), and combinations of the endocytic proteins Dynamin, Nervous Wreck, EndoA and Dap160, followed by Airyscan confocal microscopy and analyses of protein levels and distribution. First, we determined recruitment or retention of endocytic machinery at the terminal by measuring their mean intensity within the entire volume of the terminal. Second, to quantify deployment to the periactive zone, we used an established workflow to segment NMJs into single synaptic units composed of a periactive zone surrounding a center region containing Brp objects (***Figure 1—figure supplement 2C***; ***Del Signore et al., 2023***). Each unit is divided into 'mesh' and

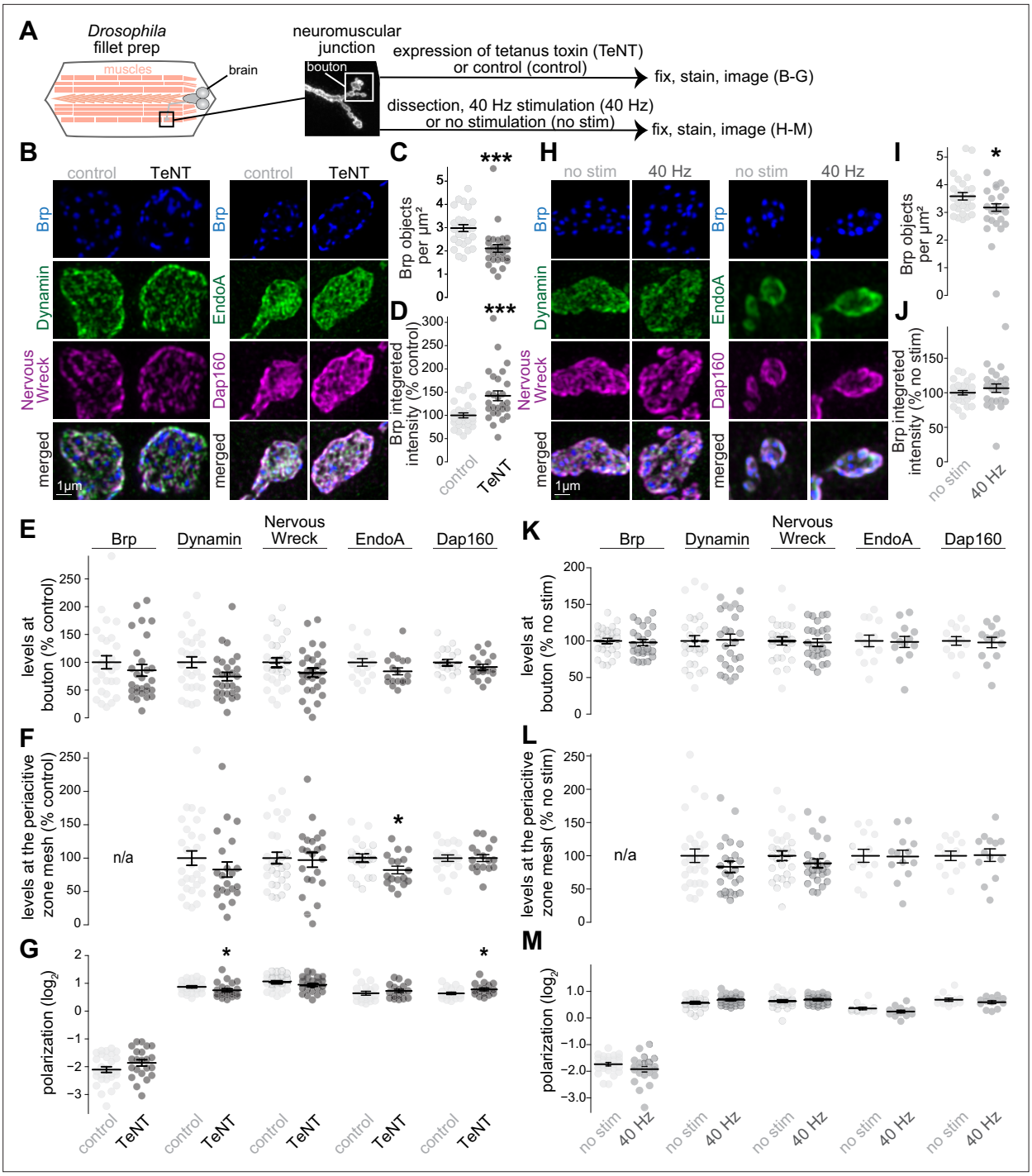

Figure 3. Deployment of endocytic proteins after chronic silencing or acute stimulation of *Drosophila* NMJs. (**A**) Schematic of the experiment at the *Drosophila* neuromuscular junction (NMJ). To silence neurons chronically, tetanus neurotoxin light chain ('TeNT') was expressed in Type 1b motor neurons on muscle 1 using the GAL4 UAS system. These neurons were compared to those from larvae expressing the M11b-GAL4 driver alone ('control'). To activate neurons, electrical stimulation was applied at 40 Hz for 3 min ('40 Hz') to Type 1b motor neurons on muscles 4 and 6/7, and comparisons were made to the contralateral, unstimulated side ('no stim'). (**B–G**) Example maximum intensity projections of ventral half of individual boutons with or without TeNT-expression stained for Brp, Dynamin and Nervous Wreck or Brp, EndoA, and Dap160 (**B**), and quantification of the number of Brp objects per µm² of NMJ (**C**) and their integrated intensity (**D**). For Brp, Dynamin, Nervous Wreck, EndoA, and Dap160, the average fluorescence intensity per bouton (**E**), the average intensity at the periactive zone mesh (**F**) and the polarization within periactive zone units (**G**) were quantified; n in C,D (NMJs/larvae): control 28/5, TeNT 27/6; E for Nervous Wreck, Dynamin, and Brp: control 28/5, TeNT 28/6; E for Dap160 and EndoA: control 19/6, TeNT 18/6; F,G for Nervous Wreck, Dynamin, and Brp: control 28/5, TeNT 22/6; F, G for Dap160 and EndoA: control 19/6, TeNT 17/6. (**H–M**) Same as

Figure 3 continued on next page

Figure 3 continued

B–G but comparing acutely stimulated ('40 Hz') and unstimulated terminals ('no stim') boutons; n in I, J: no stim 26/14, 40 Hz 24/14; K for Nervous Wreck, Dynamin, and Brp: no stim 26/14, 40 Hz 25/14; K for Dap160 and EndoA: no stim 13/7, 40 Hz 13/7; L, M for Nervous Wreck, Dynamin and Brp: no stim 26/14, 40 Hz 23/14; L, M for Dap160 and EndoA: no stim 13/7, 40 Hz 13/7. Data in D–F and J–L are normalized to the average of the control condition. Data are mean ± SEM; *p < 0.05 determined by two-sided Student's *t*-tests (E for Nervous Wreck, EndoA, and Dap160; F for EndoA and Dap160; G for Brp, Nervous Wreck, EndoA, and Dap160; I–L for EndoA and Dap160; M for Brp, Dynamin, and Nervous Wreck) or two-sided Mann–Whitney *U* tests (C–E for Brp and Dynamin; F, G for Dynamin; L, M for EndoA and Dap160). Images acquired by Airyscan microscopy, for quantification of EndoA and Dap160 using STED microscopy, see ***Figure 3—figure supplement 1***.

The online version of this article includes the following figure supplement(s) for figure 3:

Figure supplement 1. Assessment of EndoA and Dap160 after chronic silencing of *Drosophila* NMJs using STED microscopy.

'core' regions, where the periactive zone mesh is a ~175-nm wide area localized at ~330 nm from the center, and the 'core' region is the interior to this mesh (***Del Signore et al., 2023***). We estimated the levels of proteins in the periactive zone mesh as their mean intensity levels within this region and their distribution as the log ratio of the average intensity within the mesh over the core, with positive ratios indicating mesh enrichment and negative ratios indicating core enrichment (***Figure 1—figure supplement 2C***). As reported previously (***Akbergenova et al., 2025***), TeNT expression resulted in fewer Brp objects per μm^2 of NMJ and an increase in their integrated intensity (***Figure 3B–D***). However, TeNT expression did not alter the total levels of Nervous Wreck, Dynamin, EndoA, or Dap160, and only resulted in a small decrease of the levels of EndoA at the periactive zone mesh, and in small changes in the polarization of Dynamin and Dap160 (***Figure 3E–G***). A separate experiment in which we imaged EndoA and Dap160 in these conditions using STED microscopy rendered the same conclusion (***Figure 3—figure supplement 1***), supporting the model of activity-independent recruitment of endocytic proteins at *Drosophila* NMJs.

We next tested the prediction that enhanced activity might increase the localization of endocytic proteins to the periactive zone at the *Drosophila* NMJ. To do so, we electrically stimulated Type 1b motor neurons on muscles 4 and 6/7 with a 3 min 40 Hz train (***Figure 3A***), a stimulus which induces endocytosis and causes redistribution of $PI(4,5)P_2$ at the presynaptic membrane (***Li et al., 2020***). If deployment were enhanced by activity, we would expect increased periactive zone targeting of endocytic proteins and a concomitant increase in their polarization. However, we only observed an effect on the number of Brp objects, and saw no changes in the levels of Dynamin, Nervous Wreck, EndoA or Dap160 at boutons or at periactive zones, and no changes in the polarization of these proteins (***Figure 3H–M***).

Altogether, we conclude that evoked neurotransmission is not necessary to target endocytic machinery to NMJs or to localize them within boutons, nor does enhanced activity in the tested paradigms boost their periactive zone localization.

Efficient deployment of endocytic proteins after Ca_V2 ablation in mouse hippocampal neurons

Action potential-triggered fusion of synaptic vesicles depends on Ca^{2+} influx via voltage-gated Ca^{2+} channels of the Ca_V2 family (***Cao et al., 2004***; ***Cunningham et al., 2022***; ***Held et al., 2020***). As a complementary approach to study the role of synaptic activity in the recruitment of endocytic machinery, we assessed synapses lacking Ca_V2s (***Figure 4A***). We cultured neurons from previously generated triple conditional Ca_V2 knockout mice ($Ca_V2.1$, $Ca_V2.2$, and $Ca_V2.3$) and used lentiviral transduction to express Cre recombinase to generate Ca_V2 triple knockout ($cTKO^{Cav2}$) neurons. This disrupts action potential-evoked exocytosis (***Chin and Kaeser, 2024***; ***Held et al., 2020***). We expressed a recombination-deficient Cre enzyme that is truncated to generate control ($control^{Cav2}$) neurons (***Held et al., 2020***). In confocal microscopic images, the average synaptic signal intensities of Amphiphysin, PIPK1γ, AP-180, and Dynamin-1 were intact at $cTKO^{Cav2}$ synapses (***Figure 4—figure supplement 1***), confirming efficient targeting of these proteins. No major changes in their subsynaptic localization were observed. When assessed in STED microscopic images, the axial protein distributions of Amphiphysin, PIPK1γ, AP-180, and Dynamin-1 were unchanged at $cTKO^{Cav2}$ synapses, and the peak fluorescence intensities within the periactive zone region of $cTKO^{Cav2}$ synapses were within ~10% of the intensities measured at $control^{Cav2}$ synapses (***Figure 4B–K***, ***Figure 4—figure supplement 2***). At

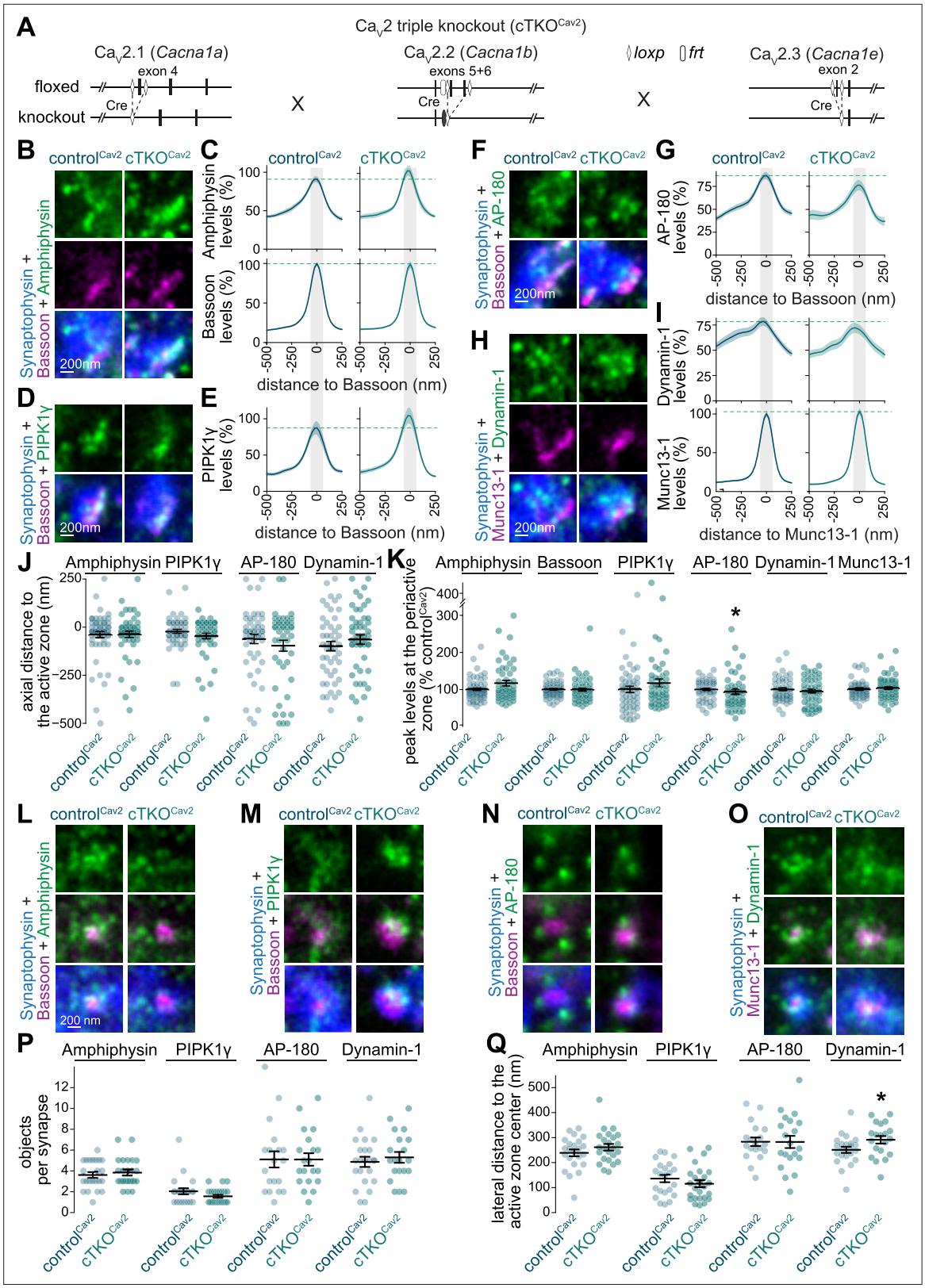

Figure 4. Deployment of endocytic proteins after Ca$_V$2 ablation in mouse hippocampal neurons. (**A**) Schematics of the *Cacna1a*, *Cacna1b*, and *Cacna1e* mutant alleles that constitute the conditional Ca$_V$2 triple knockout mouse line as described in ***Held et al., 2020***. (**B–I**) Example side-view synapses and average line profiles of Amphiphysin and Bassoon (**B, C**), PIPK1γ (**D, E**), AP-180 (**F, G**), and Dynamin-1 and Munc13-1 (**H, I**). Neurons were stained for a protein of interest (Amphiphysin, PIPK1γ, AP-180, or Dynamin-1; imaged in STED), an active zone marker (Bassoon or Munc13-1; imaged in STED),

Figure 4 continued on next page

Figure 4 continued

and Synaptophysin (imaged in confocal). An area of interest was positioned perpendicular to the center of the active zone marker, and synapses were aligned via the peak fluorescence of the active zone marker in the average profiles (**C, E, G, I**). Line profile plots were normalized to the average signal in the control^{Cav2} condition. Dashed lines in C, E, G, and I mark average levels in the control^{Cav2} condition, and gray shaded areas represent the active zone and periactive zone area; n in B, C (synapses/cultures): control^{Cav2} 58/3, cTKO^{Cav2} 50/3; D, E: control^{Cav2} 50/3, cTKO^{Cav2} 49/3; F, G: control^{Cav2} 50/3, cTKO^{Cav2} 47/3; H, I: control^{Cav2} 48/3, cTKO^{Cav2} 50/3. (**J, K**) Quantification and statistical analyses of the experiment shown in B–I, including peak-to-peak distance of the active zone marker and the protein of interest (**J**), and of the peak intensity in the periactive zone area (**K**). The periactive zone area is defined as an area within 68 nm on each side of the peak of the active zone marker (gray shaded areas in **C, E, G, I**); n as in B–I. (**L–Q**) Example en-face synapses (**L–O**) and quantification of the number of objects (**P**) and distance of these objects to the center of the active zone marker (**Q**) of the experiment shown in B–L; n in P, Q: Amphiphysin, control^{Cav2} 23/3, cTKO^{Cav2} 24/3; PIPK1γ, control^{Cav2} 22/3, cTKO^{Cav2} 25/3; AP-180, control^{Cav2} 19/3, cTKO^{Cav2} 20/3; Dynamin-1, control^{Cav2} 23/3, cTKO^{Cav2} 20/3. Data are mean ± SEM; *p < 0.5 determined by two-sided Student's *t*-tests (J for Dynamin-1; K for Dynamin-1; P for PIPK1γ and Dynamin; Q for Amphiphysin, AP-180, and Dynamin-1) or two-sided Mann–Whitney *U* tests (J for Amphiphysin, PIPK1γ, and AP-180; K for Amphiphysin, Bassoon, PIPK1γ, AP-180, and Munc13-1; P for Amphiphysin and AP-180; Q for PIPK1γ). For quantification of confocal signals, see ***Figure 4—figure supplement 1***; for assessment of AP-180 using an independent antibody, see ***Figure 4—figure supplement 2***; for additional assessment of en-face synapses, see ***Figure 4—figure supplement 3***.

The online version of this article includes the following figure supplement(s) for figure 4:

Figure supplement 1. Confocal microscopic analyses of synapses after Ca_V2 ablation in mouse hippocampal neurons.

Figure supplement 2. Assessment of AP-180 with an alternate antibody after Ca_V2 ablation in mouse hippocampal neurons.

Figure supplement 3. Additional analyses of en-face synapses after Ca_V2 ablation in mouse hippocampal neurons.

en-face synapses, the number and intensity of clusters positioned at 100–300 nm from the active zone center were unchanged (***Figure 4L–Q***, ***Figure 4—figure supplement 3***).

We conclude that ablating Ca_V2s to disrupt action potential-induced synaptic vesicle exocytosis does not impair the localization of endocytic proteins, matching the outcomes of the pharmacological inhibition experiments.

Deployment of endocytic proteins after active zone disruption in mouse hippocampal neurons

The active zone generates sites for synaptic vesicle fusion and clusters Ca_V2 channels at the presynaptic plasma membrane (***Emperador-Melero and Kaeser, 2020***; ***Südhof, 2012***). It is a multiprotein machinery formed by RIM, RIM-BP, Liprin-α, Munc13, ELKS, Piccolo/Bassoon, and other proteins that is subdivided into distinct sub-machineries (***Acuna et al., 2016***; ***Aravamudan et al., 1999***; ***Biederer et al., 2017***; ***Böhme et al., 2016***; ***Emperador-Melero et al., 2024***; ***Emperador-Melero et al., 2021b***; ***Emperador-Melero and Kaeser, 2020***; ***Graf et al., 2012***; ***Kaufmann et al., 2002***; ***Kittel et al., 2006***; ***Liu et al., 2011***; ***Marcó de la Cruz et al., 2024***; ***McDonald et al., 2020***; ***Südhof, 2012***; ***Wang et al., 2016***; ***Zhen and Jin, 1999***). Endocytic machineries are localized adjacent to active zones, and the functions of these two machineries are coordinated. Hence, their assembly may be linked with instructive roles of the active zone. To test this hypothesis, we used quadruple conditional ablation of RIM1, RIM2, ELKS1, and ELKS2 at hippocampal synapses. At these synapses, active zone assembly is strongly impaired with disrupted localization of Munc13, Piccolo/Bassoon, RIM-BP, and Ca_V2 (***Emperador-Melero et al., 2024***; ***Tan et al., 2022***; ***Wang et al., 2016***; ***Wong et al., 2018***). We cultured neurons from these mice and transduced them with lentiviruses expressing Cre or inactive Cre to produce RIM + ELKS quadruple knockout (cQKO^{R+E}) or control neurons (control^{R+E}), respectively (***Figure 5A***). We antibody-stained these cultures as in ***Figures 1 and 4***, but used the postsynaptic marker PSD-95 instead of an active zone marker because the active zone is disrupted at cQKO^{R+E} synapses. At side-view synapses, PSD-95 is localized apposed to active zones at a distance of ~75 nm (***Emperador-Melero et al., 2024***; ***Emperador-Melero et al., 2021b***; ***Held et al., 2020***; ***Tan et al., 2022***; ***Tang et al., 2016***; ***Wong et al., 2018***). Altogether, endocytic machinery remained correctly localized after active zone disruption. In confocal images (***Figure 5—figure supplement 1***), average intensities of fluorescence signals for antibody staining for Amphiphysin, PIPK1γ, AP-180, and Dynamin-1 at presynapses were either similar or higher in cQKO^{R+E} neurons. At side-view synapses in STED microscopy (***Figure 5B–L***, ***Figure 5—figure supplement 2***), the peak intensities were at a similar distance from PSD-95, and the signals within the region corresponding to the periactive zone were either higher or unchanged. Similarly, endocytic proteins at en-face synapses (***Figure 5M–R***, ***Figure 5—figure supplement 3***) from cQKO^{R+E} neurons were organized into clusters with comparable

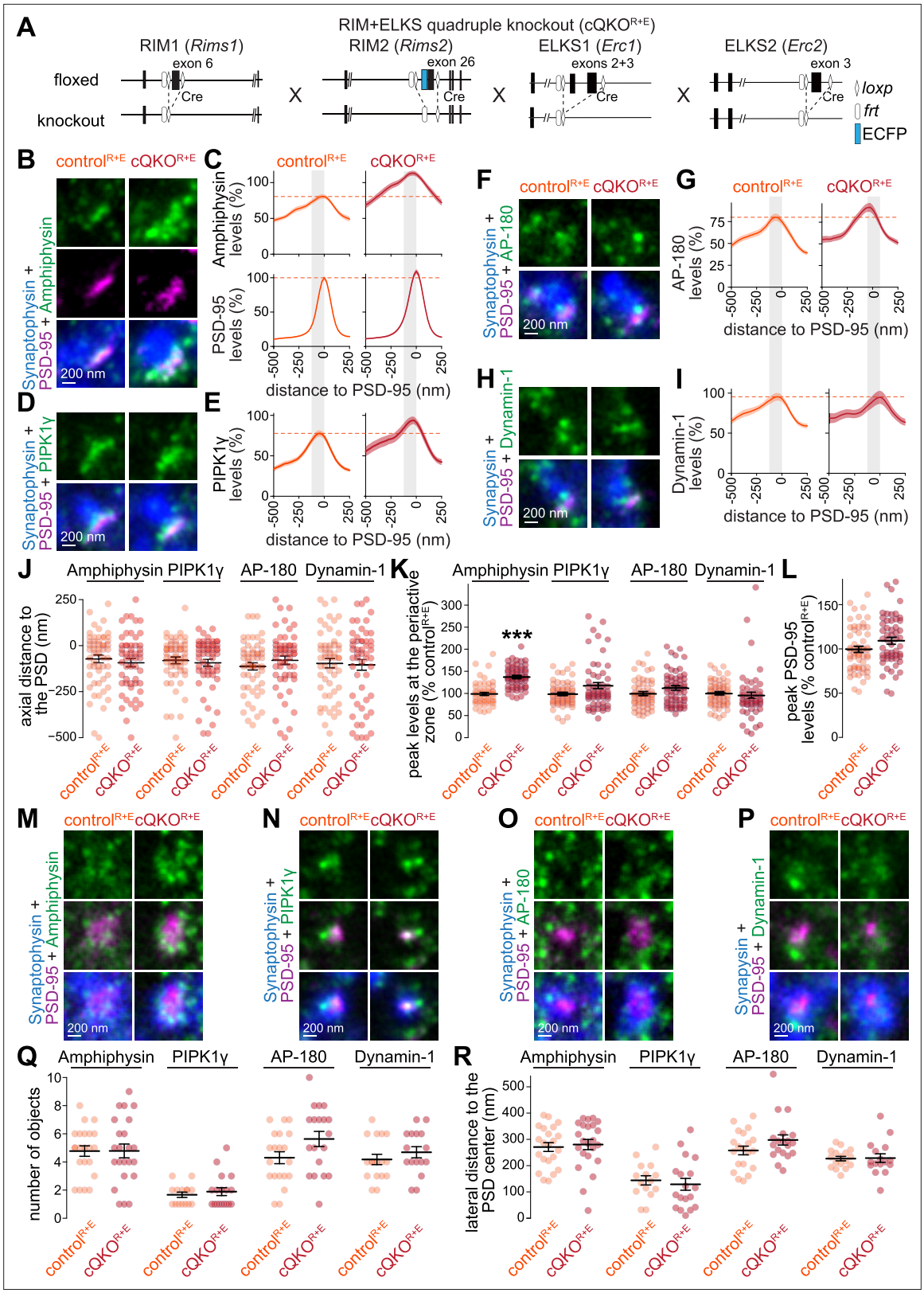

Figure 5. Recruitment of endocytic proteins to the periactive zone after active zone disruption in mouse hippocampal neurons. (**A**) Schematics of the *Rims1*, *Rims2*, *Erc1*, and *Erc2* mutant alleles that constitute the conditional RIM +ELKS quadruple knockout mouse line as described in ***Tan et al., 2022***; ***Wang et al., 2016***. (**B–I**) Example side-view synapses and average line profiles of Amphiphysin and PSD-95 (**B, C**), PIPK1γ (**D, E**), AP-180 (**F, G**), and Dynamin-1 (**H, I**). Neurons were stained for a protein of interest (Amphiphysin, PIPK1γ, AP-180, or Dynamin-1; imaged in STED), a postsynaptic

Figure 5 continued on next page

Figure 5 continued

marker (PSD-95; imaged in STED), and a synaptic vesicle marker (Synaptophysin or Synapsin; imaged in confocal). An area of interest was positioned perpendicular to the center of the PSD-95 object, and synapses were aligned via the peak fluorescence of PSD-95 in the average line profiles (**C, E, G, I**). Line profile plots were normalized to the average signal in the control^{R+E} condition. Dashed lines in C, E, G, and I mark average levels in the control^{R+E} condition and gray shaded areas represent the active zone and periactive zone area; n in B, C (synapses/cultures): control^{R+E} 55/3, cQKO^{R+E} 53/3; D, E: control^{R+E} 55/3, cQKO^{R+E} 54/3; F, G: control^{R+E} 53/3, cQKO^{R+E} 54/3; H, I: control^{R+E} 54/3, cQKO^{R+E} 53/3. (**J–L**) Quantification and statistical analyses of the experiment shown in B–I, including-to-peak distance of PSD-95 and the protein of interest (**J**), peak intensity in the periactive zone area (**K**), and peak intensity of PSD-95 (**L**). The periactive zone area is defined as an area between –136 nm and the peak of PSD-95 (gray shaded areas in **C, E, G, I**); n as in B–I. (**M–R**) Example en-face synapses (**M–P**) and quantification of the number of objects (**Q**) and distance of these objects to the center of the PSD-95 object (**R**) of the experiment shown in B–L; n in Q, R: Amphiphysin, control^{R+E} 22/3, cQKO^{R+E} 23/3; PIPK1γ control^{R+E} 15/3, cQKO^{R+E} 18/3; AP-180 control^{R+E} 20/3, cQKO^{R+E} 19/3; Dynamin-1 control^{R+E} 17/3, cQKO^{R+E} 16/3. Data are mean ± SEM; ***p < 0.001 as determined by two-sided Student's *t*-tests (L, Q for Amphiphysin, AP-180, and Dynamin-1; R for PIPK1γ and Dynamin-1) or two-sided Mann–Whitney *U* tests (J, K, Q for PIPK1γ; R for Amphiphysin and AP-180). For quantification of confocal signals, see ***Figure 5—figure supplement 1***; for assessment of AP-180 using an independent antibody, see ***Figure 5—figure supplement 2***; for additional assessment of en-face synapses, see ***Figure 5—figure supplement 3***.

The online version of this article includes the following figure supplement(s) for figure 5:

Figure supplement 1. Additional analyses of endocytic proteins after active zone disruption in mouse hippocampal neurons.

Figure supplement 2. Assessment of AP-180 with an alternate antibody after active zone disruption in mouse hippocampal neurons.

Figure supplement 3. Additional analyses of en-face synapses after active zone disruption in mouse hippocampal neurons.

localization and similar or greater integrated density. We conclude that the localization of endocytic proteins to the periactive zone is not impaired after disrupting active zone assembly through knockout of RIM and ELKS.

Deployment of endocytic proteins at *Drosophila* NMJs after disrupting active zone assembly

The active zone of the *Drosophila* NMJ has a T-bar, a prominent electron-dense invagination consisting mainly of Brp (***Fouquet et al., 2009***; ***Kittel et al., 2006***; ***Wagh et al., 2006***). Brp is required for the normal clustering of Ca_V2 Ca^{2+} channels at the active zone, and its ablation severely decreases evoked release (***Fouquet et al., 2009***; ***Kittel et al., 2006***; ***Wagh et al., 2006***). To determine whether these defects perturb periactive zone protein recruitment, we analyzed levels and localization of endocytic proteins in *brp* mutants (***Figure 6A***). After genetic ablation of *brp*, the levels of Dynamin and Nervous Wreck at NMJs were not decreased, and these proteins remained concentrated in the periactive zone mesh (***Figure 6B–E***). These data indicate that Brp and active zone T-bars are dispensable for the localization of these endocytic proteins to the periactive zone at the *Drosophila* NMJ and support the finding (***Figures 1B–G and 3B–G***) that periactive zone properties do not depend on evoked release.

Deployment of endocytic machinery after disruption of upstream active zone assembly mechanisms

The observation that active zone disassembly does not reduce levels or disrupt localization of endocytic proteins at periactive zones (***Figures 5 and 6***) suggests that active zones and endocytic machineries are organized independently of one another. Alternatively, shared upstream assembly pathways might help co-organization of the active zone and the periactive zone. Liprin-α is an upstream active zone organizer that maintains priming machineries and recruits additional presynaptic material (***Böhme et al., 2016***; ***Emperador-Melero et al., 2024***; ***Emperador-Melero et al., 2021b***; ***Kaufmann et al., 2002***; ***Marcó de la Cruz et al., 2024***; ***McDonald et al., 2020***; ***Wong et al., 2018***; ***Zhen and Jin, 1999***). We assessed the localization of endocytic proteins in Liprin-α mutants to assess whether Liprin-α might co-organize active zone and periactive zone assembly. In vertebrates, four Liprin-α proteins are expressed from four different genes (***Zürner and Schoch, 2009***). We previously generated quadruple Liprin-α mutant mice containing conditional Liprin-α1, -α2, and -α4 knockout alleles and constitutive Liprin-α3 knockout alleles (***Emperador-Melero et al., 2024***; ***Emperador-Melero et al., 2021b***; ***Wong et al., 2018***). We cultured hippocampal neurons from these mice and transduced them with Cre lentivirus to produce quadruple knockout (cQKO$^{L1\text{-}L4}$) neurons, or a combination of two viruses to express Liprin-α3 and a truncated, inactive version of Cre, to generate control (control$^{L1\text{-}L4}$) neurons, as described before (***Emperador-Melero et al., 2024***). Synapses of cQKO$^{L1\text{-}L4}$ neurons have altered active zone properties, with decreased levels of RIM and Munc13-1, accompanied by

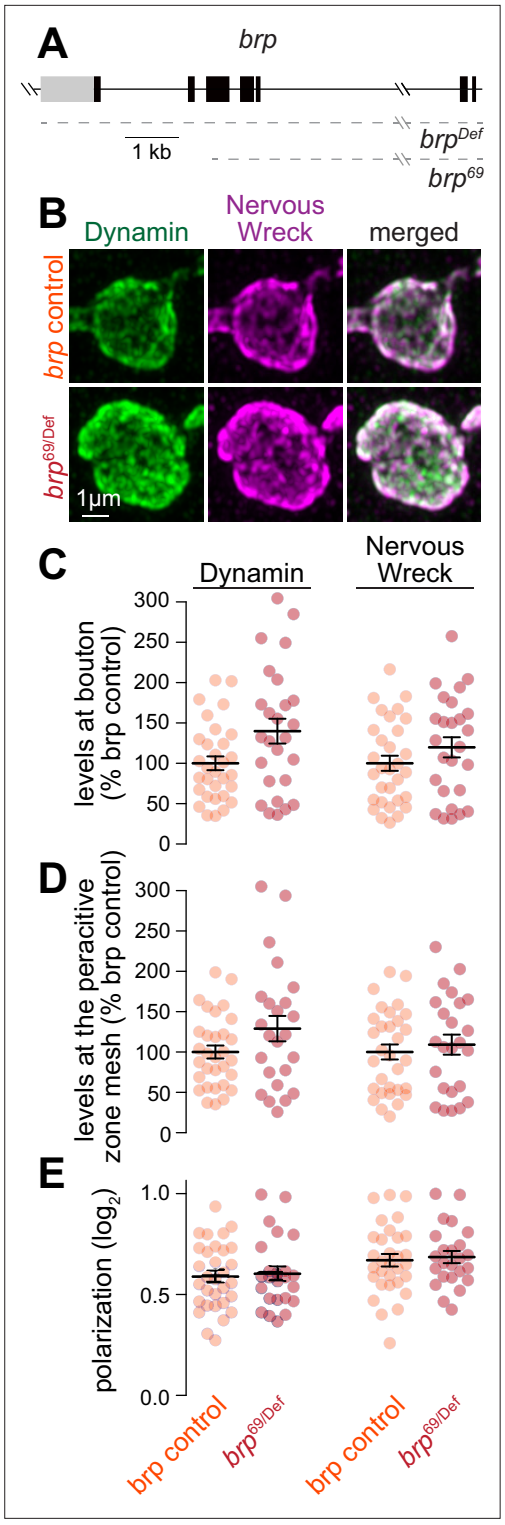

Figure 6. Recruitment of endocytic proteins to the periactive zone after disrupting active zone assembly at *Drosophila* NMJs. (**A**) Schematic of the brp^{69} and brp^{Def} alleles; dashed lines indicate the extent of deletions. (**B–E**) Example maximum intensity projections of individual boutons of muscle 4 Type 1b terminals from control *white* and brp^{69}/brp^{Def} larvae (**B**) and

Figure 6 continued on next page

Figure 6 continued

quantification of the average fluorescence intensity per bouton (**C**), average intensity at the periactive zone mesh (**D**), and polarization within periactive zone units (**E**) for Dynamin and Nervous Wreck. Data in C and D are normalized to the average control condition; n in C (NMJs/larvae): *brp* control 31/3, $brp^{69/Def}$ 26/3; D, E, *brp* control 31/3, $brp^{69/Def}$ 24/3. Data are mean ± SEM; statistical significance assessed using two-sided Student's *t*-tests (C for Nervous Wreck; D for Nervous Wreck; E for Nervous Wreck) or two-sided Mann–Whitney *U* tests (C for Dynamin; D for Dynamin; E for Dynamin). Images acquired by Airyscan microscopy.

an impairment in the readily releasable pool of synaptic vesicles (***Emperador-Melero et al., 2024***). Endocytic proteins were overall efficiently deployed to presynaptic terminals and correctly localized to the periactive zone in $cQKO^{L1\text{-}L4}$ neurons (***Figure 7***, ***Figure 7—figure supplements 1 and 2***). There were only small decreases in signal intensities generated by Amphiphysin and AP-180 antibodies, a small increase in PIPK1γ, and a modest shift in the lateral position of Amphiphysin. These results indicate that endocytic proteins are overall efficiently localized in the absence of Liprin-α proteins in mouse hippocampal neurons.

To disrupt *liprin-α* in *Drosophila*, we used a previously characterized heteroallelic mutant that results in loss-of-function of this protein ($liprin\text{-}\alpha^{EPex\text{-}R60}/liprin\text{-}\alpha^{F3ex15}$) (***Fouquet et al., 2009***; ***Kaufmann et al., 2002***; ***Owald et al., 2010***; ***Figure 8A***). Loss of *liprin-α* function reduced the overall levels of Brp at NMJs and resulted in fewer Brp puncta with a greater integrated intensity (***Figure 8B–E***) as described previously (***Fouquet et al., 2009***; ***Kaufmann et al., 2002***; ***Owald et al., 2010***). In contrast, the bouton and periactive zone levels of Dynamin, Nervous Wreck, EndoA, and Dap160 remained similar between controls and *liprin-α* mutants, though we did detect small-magnitude decreases in the polarization of Dynamin, Nervous Wreck, and Dap160 (***Figure 8E–G***). We conclude that Liprin-α does not function as a major organizer of endocytic machinery at *Drosophila* NMJs, a finding that further highlights the independence between active zone and periactive zone assembly.

As an alternative strategy to address the independence between these two machineries at the fly NMJ, we assessed the role of the synaptic vesicle-associated protein Rab3 (***Figure 9A***) using an established loss-of-function mutant ($rab3^{rup}$) (***Graf et al., 2009***; ***Peled and Isacoff, 2011***). *rab3* mutants had fewer but larger Brp objects

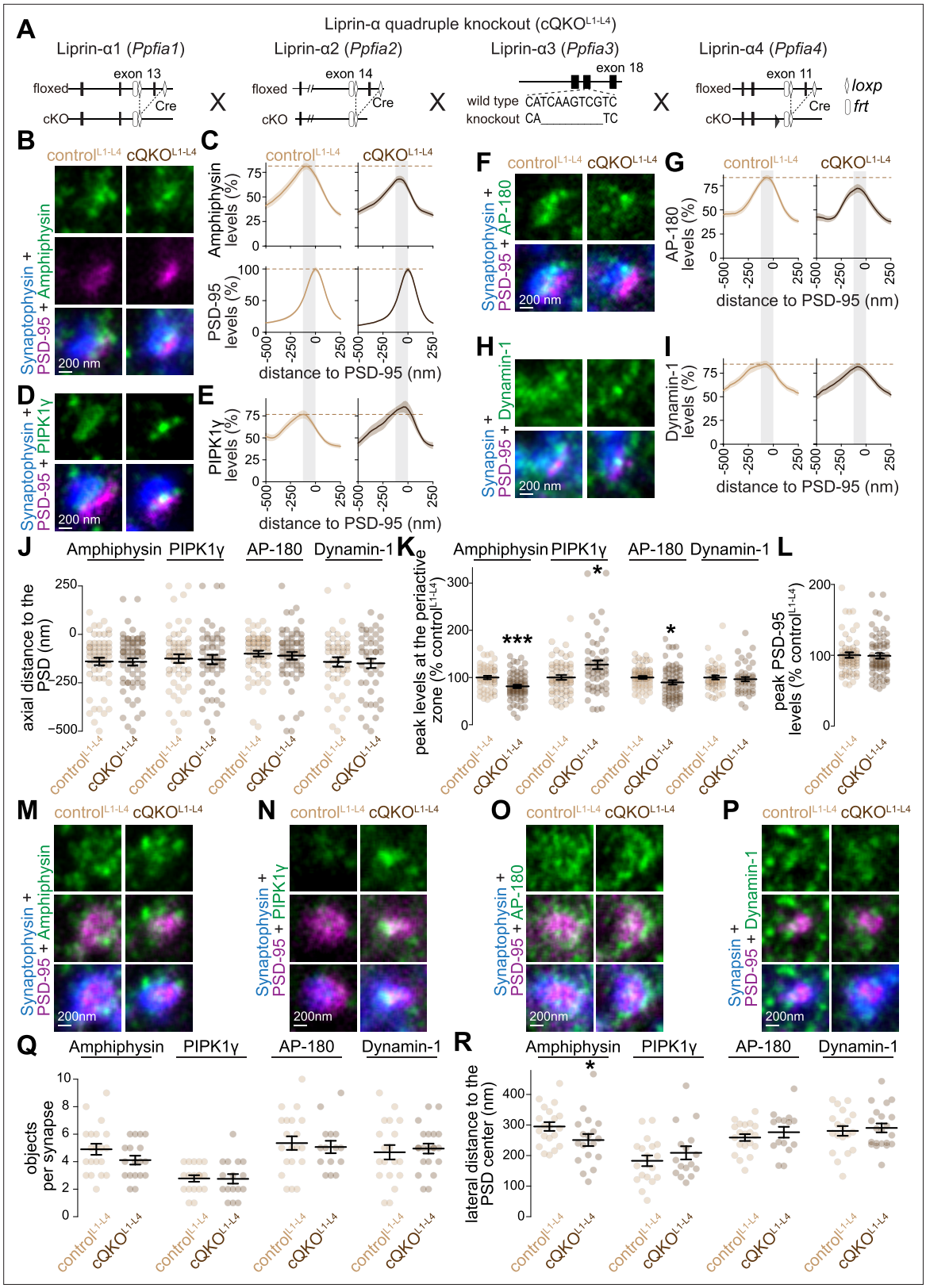

Figure 7. Deployment of endocytic proteins after Liprin-α ablation in mouse hippocampal neurons. (**A**) Schematics of the *Ppfia1*, *Ppfia2*, *Ppfia3*, and *Ppfia4* mutant alleles that constitute the conditional Liprin-α quadruple knockout mouse line as described in ***Emperador-Melero et al., 2024***. (**B–I**) Example side-view synapses and average line profiles of Amphiphysin and PSD-95 (B, C), PIPK1γ (D, E), AP-180 (F, G), and Dynamin-1 (H, I). Neurons were stained for a protein of interest (Amphiphysin, PIPK1γ, AP-180, or Dynamin-1; imaged in STED), a postsynaptic marker (PSD-95; imaged in STED),

Figure 7 continued on next page

Figure 7 continued

and a synaptic vesicle marker (Synaptophysin or Synapsin; imaged in confocal). An area of interest was positioned perpendicular to the center of the PSD-95 object, and synapses were aligned via the peak fluorescence of PSD-95 in the average profiles (**C, E, G, I**). Line profile plots were normalized to the average signal in the control$^{L1\text{-}L4}$ condition. Dashed lines in C, E, G, and I mark average levels in the control$^{L1\text{-}L4}$ condition, and gray shaded areas represent the active zone and periactive zone area; n in B (synapses/cultures), C: control$^{L1\text{-}4}$ 54/3, cQKO$^{L1\text{-}4}$ 64/3; D, E: control$^{L1\text{-}4}$ 55/3, cQKO$^{L1\text{-}4}$ 50/3; F, G: control$^{L1\text{-}4}$ 59/3, cQKO$^{L1\text{-}4}$ 59/3; H, I: control$^{L1\text{-}4}$ 45/3, cQKO$^{L1\text{-}4}$ 46/3. (**J–L**) Quantification and statistical analyses of the experiment shown in B-I, including peak-to-peak distance of PSD-95 and the protein of interest (**J**), peak intensity in the periactive zone area (**K**), and peak intensity of PSD-95 (**L**). The periactive zone area is defined as an area between –136 nm and the peak of PSD-95 (gray shaded areas in **C, E, G, I**); n as in B-I. (**M–R**) Example en-face synapses (**M–P**) and quantification of the number of objects (**Q**) and distance of these objects to the center of the PSD-95 object (**R**) of the experiment shown in B-L; n in Q, R: Amphiphysin, control$^{L1\text{-}4}$ 20/3, cQKO$^{L1\text{-}4}$ 18/3; PIPK1γ control$^{L1\text{-}4}$ 18/3, cQKO$^{L1\text{-}4}$ 16/3; AP-180 control$^{L1\text{-}4}$ 20/3, cQKO$^{L1\text{-}4}$ 15/3; Dynamin-1 control$^{L1\text{-}4}$19/3, cQKO$^{L1\text{-}4}$ 21/3. Data are mean ± SEM; *p < 0.05, ***p < 0.001 determined by two-sided Student's *t*-tests (J for PIPK1γ; K for Amphiphysin; Q for Amphiphysin, AP-180, and Dynamin-1; R for Amphiphysin, AP-180, and Dynamin-1) or two-sided Mann–Whitney *U* tests (J for Amphiphysin, AP-180, and Dynamin-1; K for PIPK1γ, AP-180, and Dynamin-1; L, Q for PIPK1γ; R for PIPK1γ). For quantification of confocal signals, see ***Figure 7—figure supplement 1***; for additional assessment of en-face synapses, see ***Figure 7—figure supplement 2***.

The online version of this article includes the following figure supplement(s) for figure 7:

Figure supplement 1. Confocal microscopic analyses of synapses after Liprin-α ablation in mouse hippocampal neurons.

Figure supplement 2. Additional analyses of en-face synapses after Liprin-α ablation in mouse hippocampal neurons.

(***Figure 9B–D***; ***Graf et al., 2009***; ***Peled and Isacoff, 2011***), though by a mechanism distinct from TeNT expression (***Akbergenova et al., 2025***). Neither the levels nor the distribution of Dynamin or Nervous Wreck were affected in *rab3* mutants (***Figure 9E–G***), showing that their periactive zone targeting is independent of *rab3*. Notably, the localization of these endocytic proteins was similar between Brp-positive and Brp-negative periactive zones in both controls and *rab3* mutants, with only modest shifts in the polarization of Dynamin in controls and of Nervous Wreck in *rab3* mutants (***Figure 9H–K***). Given the reduction in the number of Brp objects, the percentage of periactive zones without detectable Brp objects in *rab3* mutants was greater (***Figure 9L–N***). Importantly, these Brp-absent periactive zones remained apposed to the postsynaptic marker Pak (***Figure 9N***), arguing that Brp-negative periactive zones are not simply regions of membrane between adjacent periactive zones. We conclude that the recruitment of endocytic machinery does not require *rab3* and that periactive zones can be formed without an active zone.

Together, these data establish that the pathways organizing endocytic machinery are different from those organizing active zones.

Discussion

We tested the hypotheses that synaptic activity or active zone scaffolds recruit and organize endocytic machinery at the periactive zone. In mouse hippocampal neurons, neither block of action potentials and presynaptic Ca^{2+} entry nor ablation of Ca_V2s disrupted the periactive zone localization of the endocytic proteins Amphiphysin, Dynamin-1, PIPK1γ, or AP-180. Similarly, at the *Drosophila* NMJ, inhibiting evoked exocytosis did not change the levels or the subsynaptic distribution of Dynamin, Nervous Wreck, EndoA, or Dap160. These endocytic proteins also remained clustered at the periactive zone in both types of synapses when active zone assembly was disrupted via ablation of the scaffolds Brp or RIM and ELKS, or of Liprin-α or Rab3. Our data collectively argue that a periactive zone protein network, consisting of a high concentration of membrane-localized endocytic proteins, forms and is maintained independent of action potential-induced synaptic activity and active zone protein machinery.

Roles for activity in endocytic assemblies

We show that a significant fraction of endocytic proteins is already deployed to the membrane prior to stimulation. Previous experiments tested the sufficiency of depolarization to induce recruitment of endocytic machinery to the periactive zone, but not whether it is necessary (***Koh et al., 2007***; ***Winther et al., 2015***; ***Winther et al., 2013***). We found that neither continuous silencing of neurons nor ablating Ca_V2 channels resulted in decreased levels of endocytic proteins at the periactive zone. Instead, the levels of some of these proteins were increased in these conditions, the opposite of the effect expected for activity-dependent recruitment. A mechanism for this effect might be a

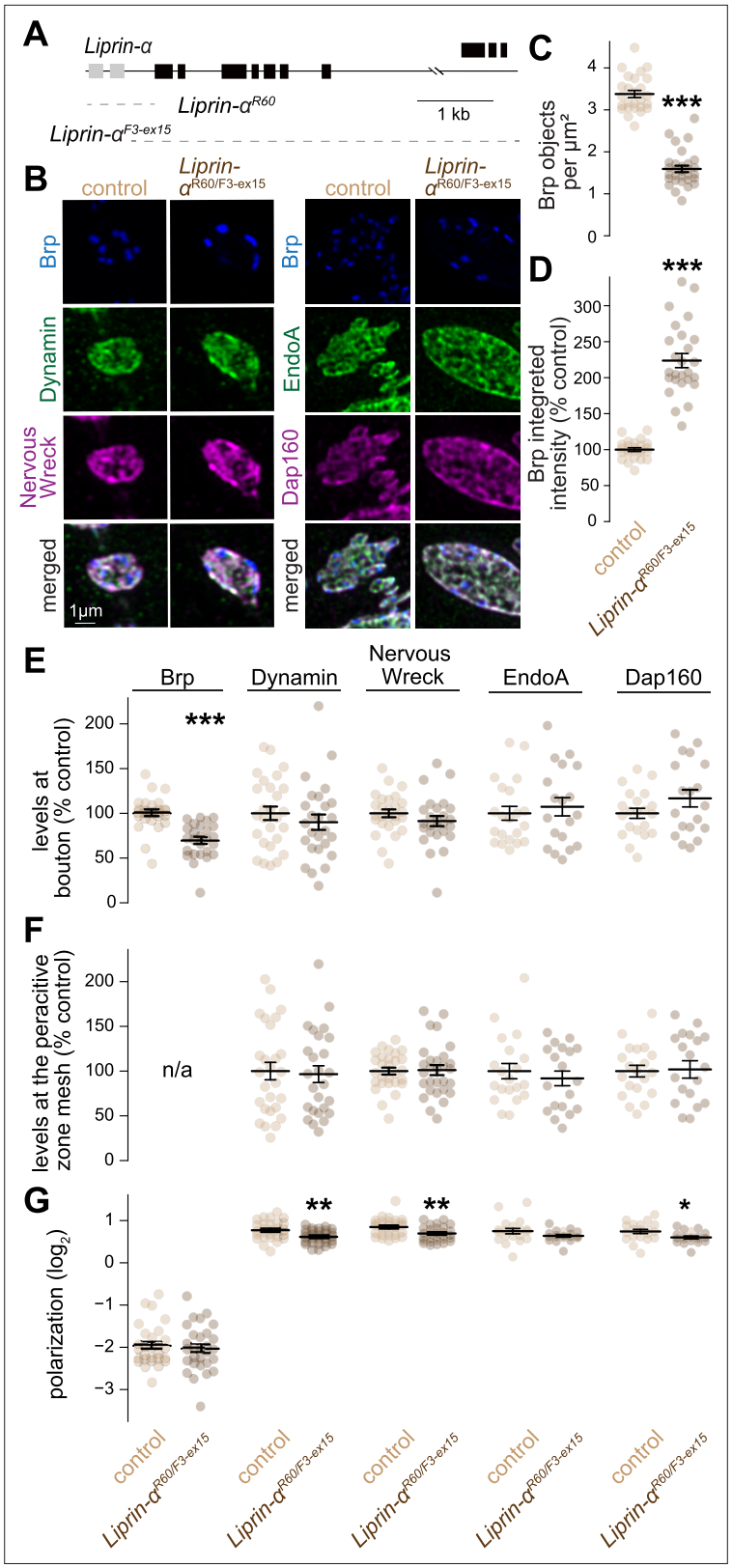

Figure 8. Endocytic proteins are recruited to periactive zones of *Drosophila* NMJs in *Liprin-α* mutants. (**A**) Schematic of the *Liprin-α*^{R60} and *Liprin-α*$^{F3\text{-}ex15}$ alleles; dashed lines indicate the extent of deletions. (**B–G**) Example maximum intensity projections of muscle 4 Type 1b terminals from *Liprin-α*$^{R60/F3\text{-}ex15}$ mutant and *white* control larvae (**B**), and quantification of the number of Brp objects per µm^2 of NMJ (**C**) and of their integrated

Figure 8 continued on next page

Figure 8 continued

intensity (**D**). For Brp, Dynamin, Nervous Wreck, EndoA, and Dap160, the average fluorescence intensity per bouton (**E**), the average intensity at the periactive zone mesh (**F**), and the polarization within periactive zone units (**G**) were quantified. Data in D, E, and F are normalized to the average of the control condition; n in C, D, and E–G for Nervous Wreck, Dynamin, and Brp (NMJs/larvae): control 27/5, *Liprin-α*$^{R60/F3\text{-}ex15}$ 26/5; E for Dap160 and EndoA: control 21/6, *Liprin-α*$^{R60/F3\text{-}ex15}$ 19/6; F, G for Dap160 and EndoA: control 20/6, *Liprin-α*$^{R60/F3\text{-}ex15}$ 19/6. Data are mean ± SEM; *p < 0.05, **p < 0.01, ***p < 0.001 determined by two-sided Student's *t*-tests (E for Dynamin and Nervous Wreck; F, G for Dynamin, EndoA, and Dap160) or two-sided Mann–Whitney *U* tests (C–E for Brp, EndoA, and Dap160; G for Brp and Nervous Wreck). Images acquired by Airyscan microscopy.

homeostatic response (***Wen and Turrigiano, 2024***) similar in magnitude to the increase in active zone protein levels following activity blockade (***Held et al., 2020***). Increased synaptic enrichment was also observed for Endophilin at nematode NMJs in mutants with disrupted exocytosis (***Bai et al., 2010***). We do not see such large shifts in Endophilin following similar manipulations, which might reflect distinct synaptic architectures in the *C. elegans* dorsal cord vs *Drosophila* NMJ terminals.

Endocytic protein recruitment and localization were largely insensitive to acute stimulation. At mouse hippocampal synapses, Dynamin-1, Amphiphysin, and PIPK1γ did not increase upon depolarization with KCl, nor did Dynamin, Nervous Wreck, EndoA, or Dap160 upon electrical stimulation of *Drosophila* NMJs. Importantly, there were varying degrees of periactive zone enrichment of endocytic proteins (***Figure 2***), and the data do not exclude the possibility that a subset of endocytic proteins is responsive to activity. In line with this, acute depolarization increased the clustering of AP-180 at periactive zones (***Figure 1***), resembling previously reported increases in Clathrin using a similar experimental paradigm (***Mueller et al., 2004***), suggesting that Clathrin and associated adapters are responsive to activity. Like the active zone (***Emperador-Melero et al., 2024***), the endocytic machinery may be formed by distinct submachineries (***Kaksonen and Roux, 2018***), which may have different degrees of constitutive deployment to the periactive zone and sensitivities to synaptic activity.

Pathways for coordinating active zone and periactive zone assembly

Despite the functional coupling of exocytosis and endocytosis in nerve terminals, it has remained unknown whether active zone proteins mediate the formation of the periactive zone. We find that ablating active zone scaffolds, upstream organizers, or Ca^{2+} channels did not disrupt the formation or structure of the periactive zone. What might be the pathways to coordinate the assembly of these two adjacent machineries? One possibility is that the co-organization of these machineries is instructed by a network of interconnected cell adhesion proteins. LAR-RPTPs and Neurexins are localized to and organize the active zone (***Emperador-Melero et al., 2024***; ***Emperador-Melero et al., 2021a***; ***Sclip and Südhof, 2023***; ***Sclip and Südhof, 2020***; ***Trotter et al., 2019***). Cell adhesion proteins localized at the edge of a synapse, such as SynCAM or Fasciclin-II (***Jiao et al., 2010***; ***Perez de Arce et al., 2015***), may play a similar role for endocytic machinery. Presynaptic cell-adhesion complexes, for example LAR-RPTPs and Neurexins, might be interlinked for the coordination of their intracellular interactors (***Thivaios et al., 2024***). Presynaptic protein complexes might also be organized via transcellular interactions, a model that is supported by our observation that periactive zones lacking Brp remain aligned with the postsynaptic marker Pak, pointing to trans-synaptic mechanisms for periactive zone organization.

Two additional contributing factors are the cytoskeleton and lipids. Multiple endocytic proteins bind to and function in the nucleation and polymerization of actin filaments (***Del Signore et al., 2021***; ***Saheki and De Camilli, 2012***; ***Stanishneva-Konovalova et al., 2016***). Interactions between several active zone proteins, such as Piccolo/Bassoon or Liprin-α, and actin regulators have also been described (***Brenig et al., 2015***; ***Terry-Lorenzo et al., 2016***), and these interactions may be important during development for the assembly of presynaptic compartments (***Chia et al., 2012***). This may explain the small decrease in the levels of Amphiphysin and AP-180 that we observed in Liprin-α null neurons. Similarly, $PI(4,5)P_2$ binds to RIM, and this interaction is critical for synaptic strength (***de Jong et al., 2018***), and the synthesis of this lipid is important for endocytosis (***Di Paolo et al., 2004***; ***Wenk et al., 2001***). Hence, actin and/or lipids may act as hubs around which active zone and endocytic machineries are organized.

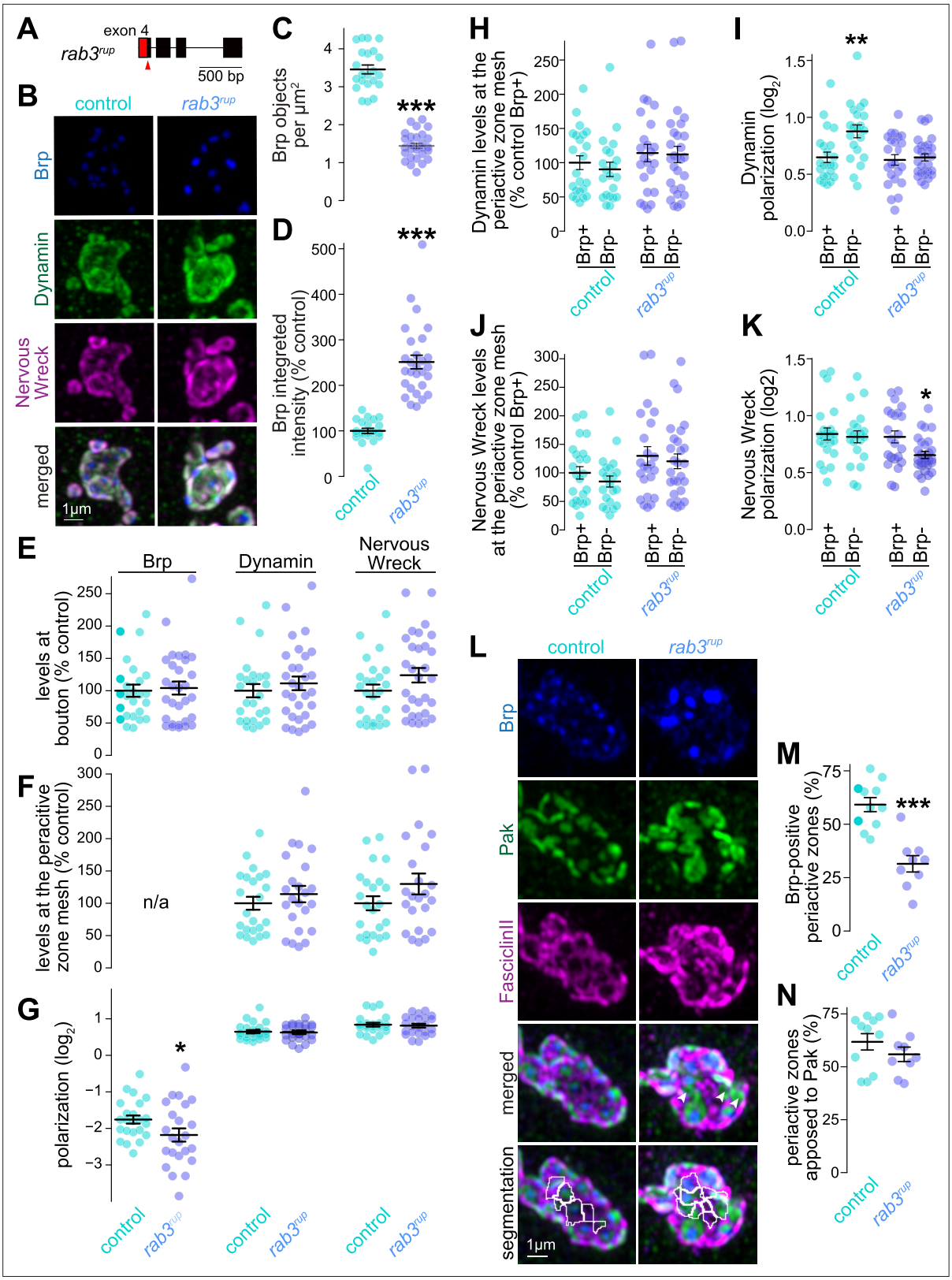

Figure 9. Recruitment of endocytic proteins at *Drosophila* NMJs in *rab3* mutants. (**A**) Schematic of the *rab3*^{rup} allele; red triangle indicates site of 5-bp deletion and frameshift that eliminates the final 35 amino acids (highlighted in red). (**B–G**) Example maximum intensity projections of muscle 4 Type 1b terminals from *rab3*^{rup} mutants and *white* larvae controls (**B**), and quantification of the number of Brp objects per µm^2 of NMJ (**C**) and of their integrated intensity (**D**). For Brp, Dynamin, and Nervous Wreck, the average fluorescence intensity per bouton (**E**), the average intensity at the periactive

Figure 9 continued on next page

Figure 9 continued

zone mesh (**F**), and the polarization within periactive zone units (**G**) were quantified. Data in D, E, and F are normalized to the average of the control condition; n in C, D (NMJs/larvae): control 22/5, *rab3*^{rup} 28/6; E: control 25/5, *rab3*^{rup} 30/6; F, G: control 23/5, *rab3*^{rup} 23/6. (**H, I**) Quantification of the levels of Dynamin (**H**) and of its polarization (**I**); n in H, I: control Brp+, 23/5, control Brp- 21/6, *rab3*^{rup} Brp +23/6, *rab3*^{rup} Brp- 28/6; (**J, K**) Same as H, I, but for Nervous Wreck; n as in H, I. (**L–N**) Example maximum intensity projections (**L**) of muscle 4 Type 1b terminals co-stained for the active-zone marker Brp, the postsynaptic density marker Pak, and the periactive zone marker Fasciclin-II (including the periactive zone segmentation, bottom image), and quantification of the percentage of individual periactive zone segments that contain Brp (**M**) or are apposed to Pak (**N**). Arrowheads point at periactive zones lacking Brp. n control 11/3, *rab3*^{rup} 9/3. Data are mean ± SEM; *p < 0.05, **p < 0.01, ***p < 0.001 determined by two-sided Mann–Whitney *U* tests (**C–G, M, N**) or by Kruskal–Wallis tests followed by Holm post hoc tests (**H–K**). In H-K, data are compared to the control Brp +condition. Images acquired by Airyscan microscopy.

Finally, interactions between endocytic proteins may further contribute to the anchoring of this apparatus. Most of these interactions are weak and transient, which may account for the high degree of turnover or mobility of these proteins at synapses (***Reshetniak et al., 2020***). However, their high concentration and their numerous interactions may suffice to maintain a stable periactive zone structure (***Saheki and De Camilli, 2012***; ***Wilhelm et al., 2014***). In support of this point, perturbing interactions between Dynamin-1 and Endophilin-A1 increases the distance between these proteins (***Imoto et al., 2024***), suggesting their binding has a scaffolding function. Ultimately, it is plausible that several or all of these pathways organize the endocytic apparatus in parallel. Redundancy is a guiding principle in the assembly of the active zone (***Acuna et al., 2016***; ***Wang et al., 2016***) and for synaptic cell adhesion (***Sclip and Südhof, 2023***), and it may similarly guide endocytic assemblies. Future studies should use loss-of-function and gene ablation approaches, including for Dynamins and other endocytic proteins, to assess roles of these pathways in presynaptic assembly.

Importance of the constitutively deployed endocytic apparatus for synapse function

The constitutive deployment of endocytic machinery to periactive zones likely enables multiple synaptic adaptations and functions of the endocytic machinery. First, ultrafast endocytosis, which occurs immediately following release (***Watanabe et al., 2014***), depends on the pre-deployment of Dynamin-1 and assembly of a periactive zone-associated ring of F-actin to facilitate membrane compression upon exocytosis (***Imoto et al., 2022***; ***Ogunmowo et al., 2023***). Pre-deployment may also facilitate vesicle recycling by limiting diffusion of synaptic vesicle cargoes (***Gimber et al., 2015***), and may be important to prevent synaptic depression (***Hua et al., 2011***; ***Kawasaki et al., 2000***; ***Moro et al., 2021***). Finally, proteins involved in endocytosis may contribute to additional functions, such as fusion of dense core vesicles, regulation of the fusion pore, and trafficking of receptors, extracellular vesicles, and cell adhesion proteins (***Anantharam et al., 2011***; ***Bailey et al., 1992***; ***Blanchette et al., 2022***; ***Fu and Huang, 2010***; ***Moro et al., 2021***; ***Rodal et al., 2008***). Thus, constitutive deployment of the endocytic machinery is likely an essential adaptation to meet the demands for fast, scalable, and robust membrane internalization during synaptic vesicle recycling and to facilitate its diverse functions at the synapse.

Given the constitutive deployment of endocytic machinery, why is it not constitutively active and continuously retrieving presynaptic plasma membrane? Plausible mechanisms may include one or more of the following factors, which might be relieved in response to Ca^{2+} entry or synaptic vesicle fusion. First, the endocytic machinery may be maintained in an inactivated state via autoinhibition of some of its components, for example, Endophilin or Nervous Wreck (***Del Signore et al., 2021***; ***Rao et al., 2010***; ***Stanishneva-Konovalova et al., 2016***). Second, endocytic proteins deployed to the periactive zone might be segregated into distinct periactive zone protein pools and thus not be able to functionally interact. In support of this model, we observed that the clustering pattern of PIPK1γ in silenced hippocampal synapses was different from that of Dynamin-1, Amphiphysin, and AP-180 (***Figure 1***). Furthermore, our previous work revealed low co-localization between Dynamin, Nervous Wreck, Dap-160, and Clathrin within periactive zones at the *Drosophila* NMJs (***Del Signore et al., 2023***). Third, one or multiple essential components of the endocytic machinery might not be predeployed to the membrane and may be delivered by an alternative mechanism (***Bai et al., 2010***). This is supported by the observation that synaptic vesicle proteins, such as Synaptotagmin-1, have a role in endocytosis (***Bolz et al., 2023***; ***Haucke and De Camilli, 1999***; ***Jorgensen et al., 1995***; ***Poskanzer***

et al., 2006; *Zhang et al., 1994*). Finally, the endocytic process may rely on a decrease in membrane tension (*Ogunmowo et al., 2023*; *Watanabe et al., 2013*) and thus require fusion for its initiation. Given the multiple mechanisms by which periactive zone proteins likely contribute to synaptic vesicle endocytosis, and considering their potential synaptic vesicle-independent functions, it is possible that constitutive deployment is a necessary synaptic adaptation of the conserved endocytic machinery. Testing whether this is the case will require identifying the mechanisms that are essential for constitutive deployment of the endocytic machinery to the periactive zone.

Limitations and outlook

The presented data indicate that evoked neurotransmission and active zone scaffolds are not required for the localization of the tested endocytic proteins to the periactive zone, but several limitations are present.

First, conclusions that can be drawn on the roles of spontaneous release in periactive zone assembly remain limited. While many of the manipulations used here, including Ca_V2 knockout (*Held et al., 2020*), RIM + ELKS knockout (*Tan et al., 2022*; *Wang et al., 2016*), and Liprin-α knockout (*Emperador-Melero et al., 2024*) in hippocampal neurons, and TeNT expression in fly NMJs (*Sweeney et al., 1995*), result in 50–70% decreased spontaneous release rates, it is possible that the remaining spontaneous release supports periactive zone assembly. Future studies might test manipulations with strong effects on miniature release, including those affecting SNARE proteins and their regulators, with the caveat that these manipulations might have effects on upstream trafficking and in some cases on cell survival (*Kaeser and Regehr, 2014*; *Santos et al., 2017*).

Second, the endocytic machinery might be sensitive to manipulations over timescales that were not included in the presented analyses. The experiments with activity induction focused on periactive zone protein enrichment immediately following stimulation and do not exclude that activity may recruit endocytic proteins over slower time scales. Likewise, our data cannot exclude localization of endocytic proteins to other axonal compartments, where they may execute functions different from endocytosis.

Finally, the studies presented here are focused on the recruitment and organization of endocytic machinery, and it was not tested whether these manipulations perturb endocytic function. Studying these deficits in mutants that alter exocytosis is complicated by the fact that synaptic endocytosis occurs following exocytosis. Furthermore, functional roles for endocytic proteins beyond endocytosis, such as those for Intersectin in vesicle clustering (*Milovanovic et al., 2018*), and of Endophilin in autophagy (*Bademosi et al., 2023*; *Soukup and Verstreken, 2017*), may also be present.

Overall, the data on endocytic protein localization argue for constitutive deployment of this protein machinery to the periactive zone. This work builds a foundation to assess alternative mechanisms and models of periactive zone assembly, including roles of the cytoskeleton, lipids, adhesion molecules, and intrinsic endocytic protein interactions.

Materials availability

Mouse lines, *Drosophila* lines, plasmids, and antibodies will be shared upon request within the limits of the existing material transfer agreements and as long as they are available. Requests for resources and reagents should be directed to the corresponding authors.

Materials and methods

Key resources table

Reagent type (species) or resource	Designation	Source or reference	Identifiers	Additional information
Genetic reagent (*Mus musculus*)	*Cacna1a* conditional knockout	*Todorov et al., 2006*		
Genetic reagent (*M. musculus*)	*Cacna1b* conditional knockout	*Held et al., 2020*		
Genetic reagent (*M. musculus*)	*Cacna1e* conditional knockout	*Pereverzev et al., 2002*		

Continued on next page

Continued

Reagent type (species) or resource	Designation	Source or reference	Identifiers	Additional information
Genetic reagent (*M. musculus*)	*Rims1* conditional knockout	**Kaeser et al., 2008**	RRID:IMSR_JAX:015832	
Genetic reagent (*M. musculus*)	*Rims2* conditional knockout	**Kaeser et al., 2011**	RRID:IMSR_JAX:015833	
Genetic reagent (*M. musculus*)	*Erc1* conditional knockout	**Liu et al., 2014**	RRID:IMSR_JAX:015830	
Genetic reagent (*M. musculus*)	*Erc2* conditional knockout	**Kaeser et al., 2009**	RRID:IMSR_JAX:015831	
Genetic reagent (*M. musculus*)	*Ppfia1* conditional knockout	**Emperador-Melero et al., 2024**	RRID:IMSR_EUMMCR:25506	
Genetic reagent (*M. musculus*)	*Ppfia2* conditional knockout	**Emperador-Melero et al., 2021b**	RRID:IMSR_HAR:6799	
Genetic reagent (*M. musculus*)	*Ppfia3* constitutive knockout	**Wong et al., 2018**		
Genetic reagent (*M. musculus*)	*Ppfia4* conditional knockout	**Emperador-Melero et al., 2024**	RRID:IMSR_EUMMCR:3103	
Cell line (*Homo sapiens*)	HEK 293T cells	ATCC	Cat# CRL-3216; RRID:CVCL_0063	
Recombinant DNA reagent	pFSW HA-Liprin-α3 (plasmid)	**Wong et al., 2018**	p526	
Recombinant DNA reagent	pFSW (plasmid)	**Nyitrai et al., 2020**	p008	
Recombinant DNA reagent	pFSW GFP Cre (plasmid)	**Kaeser et al., 2011**	p009	
Recombinant DNA reagent	pFSW GFP inactive Cre (plasmid)	**Kaeser et al., 2011**	p010	
Antibody	anti-Dynamin-1 (Mouse polyclonal)	**Milosevic et al., 2011**		IF (1:50)
Antibody	anti-Amphiphysin (Rabbit polyclonal)	**Di Paolo et al., 2002**		IF (1:200)
Antibody	anti-PIPK1γ (Rabbit polyclonal)	**Wenk et al., 2001**		IF (1:500)
Antibody	anti-AP180 (Mouse monoclonal)	**Koo et al., 2015**		IF (1:500)
Antibody	anti-AP180 (Rabbit polyclonal)	SySy	RRID:AB_887691	IF (1:500)
Antibody	anti-Munc13-1 (Rabbit polyclonal)	SySy	RRID:AB_887733	IF (1:500)
Antibody	anti-Synaptophysin (Mouse monoclonal)	SySy	RRID:AB_887824	IF (1:500)
Antibody	anti-Bassoon (Mouse monoclonal)	Enzo	RRID:AB_11181058	IF (1:500)
Antibody	anti-PSD-95 (Mouse monoclonal)	Neuromab	RRID:AB_10698024	IF (1:500)
Antibody	anti-PSD-95 (Guinea pig monoclonal)	SySy	RRID:AB_2619800	IF (1:500)
Antibody	anti-Gephyrin (Mouse monoclonal)	SySy	RRID:AB_2232546	IF (1:500)
Antibody	anti-Synapsin-1 (Rabbit polyclonal)	SySy	RRID:AB_2200097	IF (1:500)

Continued on next page

Continued

Reagent type (species) or resource	Designation	Source or reference	Identifiers	Additional information
Antibody	anti-Nervous Wreck 970 (Rabbit polyclonal)	***Coyle et al., 2004***	RRID:AB_2567353	IF (1:1000)
Antibody	anti-Dynamin (Guinea Pig polyclonal)	Provided by Dion Dickman		IF (1:1000)
Antibody	anti-Brp nc82 (Mouse monoclonal)	Developmental Studies Hybridoma Bank (DSHB)	RRID:AB_2314866	IF (1:1000)
Antibody	anti-Pak (Rabbit polyclonal)	***Harden et al., 1996***		IF (1:1000)
Antibody	anti-Synapsin (Mouse monoclonal)	Developmental Studies Hybridoma Bank (DSHB)	RRID:AB_528479	IF (1:100)
Antibody	anti-EndoA (Rabbit polyclonal)	Provided by Dion Dickman		IF (1:1000)
Antibody	anti-Dap160 (Guinea Pig polyclonal)	This study		IF (1:1000)
Chemical compound, drug	ω-Agatoxin IVA	Alomone labs	Cat# STA-500	200 nM
Chemical compound, drug	ω-Conotoxin GVIA	Alomone labs	Cat# C-300	250 nM
Chemical compound, drug	Tetrodotoxin	Tocris Bioscience	Cat# 1078	1 µM
Genetic reagent (*Drosophila melanogaster*)	*GMR94G06-GAL4*	Bloomington *Drosophila* Stock Center (BDSC); ***Jenett et al., 2012***	RRID:BDSC_40701	
Genetic reagent (*Drosophila melanogaster*)	*UAS-TeTxLC; UAS-TeNT*	BDSC	RRID:BDSC_28838	
Genetic reagent (*Drosophila melanogaster*)	*brpDf/CyOGFP*	***Akbergenova et al., 2018***		
Genetic reagent (*Drosophila melanogaster*)	*brp69*	***Kittel et al., 2006***		
Genetic reagent (*Drosophila melanogaster*)	*rab3rup*	***Graf et al., 2009***	RRID:BDSC_78045	
Genetic reagent (*Drosophila melanogaster*)	*liprinR60*	BDSC; ***Kaufmann et al., 2002***	RRID:BDSC_8561	
Genetic reagent (*Drosophila melanogaster*)	*liprinF3ex15*	BDSC; ***Kaufmann et al., 2002***	RRID:BDSC_8563	

Mouse lines

The triple mutant mice for ablating $Ca_V2.1$ (targeting *Cacna1a*, ***Todorov et al., 2006***), $Ca_V2.2$ (targeting *Cacana1b*, ***Held et al., 2020***) and $Ca_V2.3$ (targeting *Cacana1e*, ***Pereverzev et al., 2002***) have been previously described (***Chin and Kaeser, 2024***; ***Held et al., 2020***). Quadruple mutant mice for ablating RIM1 (targeting *Rims1* to remove RIM1α and RIM1β, ***Kaeser et al., 2008***; RRID:IMSR_JAX:015832), RIM2 (targeting *Rims2* to remove RIM2α, RIM2β, and RIM2γ, ***Kaeser et al., 2011***; RRID:IMSR_JAX:015833), ELKS1α (targeting *Erc1* to remove ELKS1αA and ELKS1αB, ***Liu et al., 2014***; RRID:IMSR_JAX:015830), and ELKS2α (targeting *Erc2* to remove ELKS2αA and ELKS2αB, ***Kaeser et al., 2009***; RRID:IMSR_JAX:015831) were previously described (***Emperador-Melero et al., 2024***; ***Tan et al., 2022***; ***Wang et al., 2016***). Quadruple mutant mice for ablating Liprin-α1 (targeting *Ppfia1*, ***Emperador-Melero et al., 2024***; RRID:IMSR_EUMMCR:25506), Liprin-α2 (targeting Ppfia2, ***Emperador-Melero et al., 2021b***; RRID:IMSR_HAR:6799), Liprin-α3 (targeting *Ppfia3*, ***Wong et al., 2018***), and Liprin-α4 (targeting *Ppfia4*, ***Emperador-Melero et al., 2024***; RRID:IMSR_EUMMCR:3103) were previously described (***Emperador-Melero et al., 2024***). Mouse lines were maintained as homozygotes for the respective mutations, and offsprings were weaned at ~21–28 days. Mice were kept separated by sex or housed as breeding pairs in a room with a regular dark light cycle and set to 22°C (range 20–24°C) and 50% humidity (range 35–70%). Animal experiments were approved by the Harvard University Animal Care and Use Committee (protocol number IS00000049).

Primary mouse hippocampal cultures

Primary hippocampal cultures were prepared using previously established protocols (***Emperador-Melero et al., 2024***; ***Held et al., 2020***; ***Nyitrai et al., 2020***; ***Wang et al., 2016***; ***Wong et al., 2018***). Hippocampi dissected from newborn pups (P0–P1) were digested in papain and dissociated. Dissociated cells were plated onto 12 mm, #1.5 glass coverslips in 'plating medium' that contained Minimum Essential Medium (MEM) supplemented with 0.5% glucose, 0.02% $NaHCO_3$, 0.1 mg/ml transferrin, 10% Fetal Select bovine serum (Atlas Biologicals FS-0500-AD), 2 mM L-glutamine, and 25 mg/ml insulin. Twenty-four hours after plating, the medium was exchanged with 'growth medium' that contained MEM with 0.5% glucose, 0.02% $NaHCO_3$, 0.1 mg/ml transferrin, 5% Fetal Select bovine serum (Atlas Biologicals FS-0500-AD), 2% B-27 supplement, and 0.5 mM L-glutamine. At 48–60 hr after plating, cytosine β-D-Arabinofuranoside (AraC) was added at a final concentration of 2–6 µM depending on glial growth. Cells were kept in an incubator at 37°C until DIV15 to DIV16. For activity blockade, a cocktail of drugs containing TTX, ω-Agatoxin IVA (ω-Aga), and ω-Conotoxin GVIA (ω-Cono) was added at DIV3 to a final concentration of 1 µM, 250 nM, and 200 nM, respectively, and supplemented every 3 days. KCl was added to a final concentration of 50 mM from a 10X stock for 30 s before fixation.

Cell lines

HEK293T cells, an immortalized cell line of female origin, were purchased from ATCC (CRL-3216, RRID:CVCL_0063) as a mycoplasma-free cell line, and were used for production of lentiviruses. These cells were maintained using established methods (***Emperador-Melero et al., 2024***; ***Held et al., 2020***; ***Nyitrai et al., 2020***; ***Wang et al., 2016***; ***Wong et al., 2018***). They were expanded and stored in liquid nitrogen until use. After thawing, cells were grown in Dulbecco's modified Eagle medium with 10% Fetal bovine serum (Atlas Biologicals F-0500-D) and 1% penicillin–streptomycin. HEK293T cells were passaged at ratios between 1:3 and 1:10 up to ~25 times, when they were replaced with a freshly thawed batch of cells.

Production of lentiviruses and transduction of primary mouse neurons

Lentiviruses were prepared using established methods (***Emperador-Melero et al., 2024***; ***Held et al., 2020***; ***Nyitrai et al., 2020***; ***Wang et al., 2016***; ***Wong et al., 2018***). HEK293T cells were transfected using the Ca^{2+} phosphate method with a combination of three packaging plasmids (REV, RRE, and VSV-G), and a lentiviral plasmid encoding either GFP-tagged Cre recombinase (Kaeser lab plasmid code p009), an inactive version of Cre (p010), Liprin-α3 (p526), or a lentivirus without an insert in the multiple cloning site (p008) at a molar ratio 1:1:1:1 and with a total amount of ~4 µg DNA per T25 flask. At 20–30 hr after transfection, the medium was changed to 'growth medium' and 48–60 hr after transfection the supernatant was collected. Viral transductions were done either with freshly collected viral supernatant or with snap-frozen supernatant stored at –80°C. Neuronal cultures were transduced with lentiviruses expressing Cre or inactive Cre at DIV2 for Ca_V2 ablation (***Held et al., 2020***), DIV5 for RIM + ELKS ablation (***Emperador-Melero et al., 2024***; ***Tan et al., 2022***; ***Wang et al., 2016***), or DIV7 for Liprin-α ablation (***Emperador-Melero et al., 2024***) following protocols established before. Transduction efficiency was monitored via the presence of nuclear GFP fluorescence, and only cultures in which no neurons without nuclear green fluorescence were readily detected were used for experiments. Liprin-α mutant neuronal cultures were additionally transduced at DIV1 with either lentivirus expressing either HA-tagged Liprin-α3 (p526; for control$^{L1\text{-}L4}$ neurons) or lentivirus without an insert in the multiple cloning site (p008; for cQKO$^{L1\text{-}L4}$ neurons). pFSW HA-Liprin-α3 (p526) corresponds in sequence and numbering to NCBI Reference Sequence: NP_001257914.1 with the addition of an N-terminal HA-tag and a short linker (sequence: M-YPYDVPDYA-GAPS-C_3…C_{1192}) and has been described before (***Emperador-Melero et al., 2024***; ***Emperador-Melero et al., 2021b***; ***Wong et al., 2018***).

Immunofluorescence staining for STED and confocal microscopy of cultured hippocampal neurons

Neurons were antibody-stained using previously established protocols (***Emperador-Melero et al., 2024***; ***Emperador-Melero et al., 2021b***; ***Held et al., 2020***; ***Wong et al., 2018***). They were fixed at DIV15 to DIV16 in PBS containing 2% PFA for 10 min at room temperature. For cultures stimulated

with KCl, 50 mM KCl was also included in the fixation solution after the 30 s depolarization described below. Neurons were blocked and permeabilized in blocking solution (PBS, 3% BSA, 0.1% Triton X-100) for 1 hr at room temperature and incubated with primary and secondary antibodies, each overnight at 4°C, in blocking solution. Three 5 min washes with PBS were performed after each antibody incubation. The cells were post-fixed in 4% PFA for 10 min, washed in PBS, and mounted using mounting medium. Primary antibodies used were: mouse anti-Dynamin-1 (Kaeser lab antibody code A242, 1:50, obtained from P. De Camilli, knockout-validated for immunostaining in ***Milosevic et al., 2011***), rabbit anti-Amphiphysin (A244, 1:200, obtained from P. De Camilli, knockout-validated for immunostaining in ***Di Paolo et al., 2002***); rabbit anti-PIPK1γ (A168, 1:500, obtained from P. De Camilli ***Wenk et al., 2001***); mouse anti-AP-180 (A246, 1:500, obtained from P. De Camilli, knockout-validated for immunostaining in ***Koo et al., 2015***); rabbit anti-AP-180 (A219, 1:500; RRID:AB_887691); rabbit anti-Munc13-1 (A72, 1:500; RRID:AB_887733); mouse anti-Synaptophysin (A100, 1:500; RRID:AB_887824); mouse anti-PSD-95 (A152, 1:500; RRID:AB_10698024); mouse anti-Bassoon (A85, 1:500; RRID:AB_11181058); guinea pig anti-PSD-95 (A5, 1:500, RRID:AB_2619800); rabbit anti-Synapsin-1 (A30, 1:500, RRID:AB_2200097); mouse anti-Gephyrin (A8; 1:500, RRID:AB_2232546). Secondary antibodies used were: goat anti-guinea pig Alexa Fluor 633 (S34; 1:250, RRID:AB_2535757), goat anti-mouse IgG2a Alexa Fluor 555 (S20; 1:250, RRID:AB_2535776), goat anti-rabbit Alexa Fluor 488 (S5; 1:250, RRID:AB_2576217), goat anti-rabbit Alexa Fluor 555 (S22; 1:250, RRID:AB_2535849), goat anti-mouse Alexa Fluor 488 (S4; 1:250, RRID:AB_2534088), goat anti-rabbit Alexa Fluor 633 (S33; 1:250, RRID:AB_2535731), and goat anti-guinea pig Alexa Fluor 555 (S23; 1:250, RRID:AB_2535856).

Image acquisition and analyses for confocal and STED microscopy of cultured hippocampal neurons

Images were acquired as previously established (***Chin and Kaeser, 2024***; ***Emperador-Melero et al., 2024***; ***Emperador-Melero et al., 2021b***; ***Emperador-Melero et al., 2021a***). A Leica SP8 Confocal/STED 3X microscope equipped with an oil-immersion 100x objective (1.44 NA), a white laser, STED gated detectors, and 592, 660, and 770 nm depletion lasers was used to acquire 2048 pixels × 2048 pixels large images (pixel size of 22.7 nm × 22.7 nm) that contained hundreds of synapses. Triple confocal scans for Synaptophysin or Synapsin, an active zone (Munc13-1 or Bassoon) or postsynaptic density (PSD-95) marker, and a protein of interest were followed by double-color STED scans for the active zone or postsynaptic density marker and the protein of interest. The exceptions were (1) combinations containing Amphiphysin and PIPK1γ in ***Figure 1***, where Synaptophysin was also imaged in STED, and (2) combinations containing Amphiphysin, PIPK1γ, or AP-180 in ***Figure 6***, where an antibody against Gephyrin was also added and imaged in confocal and STED modes as well. Acquisition settings for a given staining and channel were identical for all images within a batch of culture in which all conditions from one experiment were compared. To quantify STED images, side-view synapses were selected by an experimenter blind to the protein of interest. Side-view synapses were defined as those containing a vesicle cloud of 250 nm or more in width from the marker to the inside of the presynaptic terminal and with a bar-like Munc13-1, Bassoon, or PSD-95 structure along its edge. A 750-nm long, rectangular area of interest with a width exceeding that of the active zone or postsynaptic marker by up to five pixels on each side was drawn perpendicular to the marker and across its center. After applying a 5-pixel rolled average to the protein of interest and marker, line profiles of individual synapses were aligned to the peak of the active zone or postsynaptic marker and averaged. Next, the position of the maximum value of the endocytic protein relative to the maximum value of the marker was calculated and plotted for each synapse. The maximum fluorescence value of the endocytic protein within 136 nm relative to the peak fluorescence of the marker was also measured and plotted. For ***Figures 1 and 3***, this region spanned 68 nm at each side of the peak of the active zone marker. For ***Figures 4 and 6***, it spanned 136 nm from the PSD-95 peak toward the presynaptic bouton. These distances were chosen to match the periactive zone area based on the position of synaptic proteins at STED resolution (***Wong et al., 2018***). In each culture, line profiles and peak intensities were normalized to the average signal in the condition used for comparison (defined in the corresponding figure legend). In line profile plots, peaks are below 100% because peak intensities for proteins of interest are not always at the same position. En-face synapses were selected as synapses that did not have a bar-like appearance of the active zone or postsynaptic marker; instead, the area of the marker was surrounded by Synaptophysin or Synapsin staining. The experimenter was blind to

the protein of interest during en-face synapse selection. For any given en-face synapse, only signals of the protein of interest that fell within 136 nm of the edges of the synaptic vesicle cloud were included. This area was defined by creating a binary mask for Synaptophysin or Synapsin and expanding it by 6 pixels (each 22.7 nm). Individual channels containing the marker or the protein of interest were next thresholded. For any given experiment, thresholds were defined by an experimenter blind to the condition through visual inspection of approximately ten images, and the same thresholds were then applied to all images within an experiment. After thresholding, the 'analyze particles' function of Fiji was applied to detect individual objects and to measure their size, position, and intensity (the intensity was measured in the original, non-thresholded image). For quantification of confocal signals, individual channels were analyzed with an automatic detection algorithm (available at https://github.com/kaeserlab/3DSIM_Analysis_CL, ***Kaeserlab, 2020***). With this algorithm, Otsu thresholding was used to generate a presynaptic mask based on the Synaptophysin or Synapsin signals. The synaptic mask was subsequently used to quantify the fluorescence intensity levels of the protein of interest. To avoid detection artifacts, areas with somata and out-of-focus areas were not included in the areas of interest. Confocal data were normalized to the average in the condition that was used for comparison (noted in each figure legend) per culture. For representative images, a smooth filter was added in some cases, brightness and contrast were linearly adjusted, and images were interpolated. Identical adjustments were applied to representative images of the same channel within an experiment. Quantifications were performed on original images without brightness and contrast adjustments and without background subtraction or resampling. Data were acquired and analyzed by an experimenter blind to genotype.

Drosophila strains

Flies were cultured using standard media and techniques. All flies were raised at 25°C. Fly strains used in this work were: GMR94G06-GAL4 (RRID:BDSC_40701), UAS-TeTxLC (aka UAS-TeNT, RRID:BDSC_28838), brp^{Df} (***Akbergenova et al., 2018***), brp^{69} (***Kittel et al., 2006***), $rab3^{rup}$ (RRID:BDSC_78045 ***Graf et al., 2009***), $liprin^{R60}$ (RRID:BDSC_8561, ***Kaufmann et al., 2002***), and $liprin^{F3ex15}$ (RRID:BDSC_8563 ***Kaufmann et al., 2002***).

Generation of polyclonal antibodies

Drosophila antigens for producing anti-Dap160, anti-Dynamin, and anti-EndoA antisera were produced in lab and sent to Cocalico Biologicals, Inc (Denver, PA, USA) for injection into two guinea pigs each, and antisera were harvested. Specificity of the sera was assessed by staining NMJs of control larvae and of larvae with RNAi against the protein of interest expressed pan-neuronally by C155-Gal4 (***Figure 2—figure supplement 1***).

Guinea pig anti-Dap160 polyclonal antisera were raised against a recombinant protein fragment of *Drosophila* Dap160 SH3 domains with a 6x-His N-terminal tag (sequence: MGGSHHHHHH-GMASMTGGQQMGRDLYDDDDKDRWGSTGSSSAWEETGTTVTDPYAVASNDISALAAPAVDLGGPAPEGFVKYQAVYEFNARNAEEITFVPGDIILVPLEQNAEPGWLAGEINGHTGWFPESYVEKLEVGEVAPVAAVEAPVDAQVATVADTYNDNINTSSIPAASADLTAAGDVEYYIAAYPYESAEEGDLSFSAGEMVMVIKKEGEWWTGTIGSRTGMFPSNYVQKADVGTASTAAAEPVESLDQETTLNGNAAYTAAPVEAQEQVYQPLPVQEPSEQPISSPGVGAEEAHEDLDTEVSQINTQSKTQSSEPAESYSRPMSRTSSMTPGMRAKRSEIAQVIAPYEATSTEQLSLTRGQLIMIRKKTDSGWWEGELQAKGRRRQIGWFPATYVKVLQGGRNSGRNTPVSGSRIEMTEQILDKVIALYPYKAQNDDELSFDKDDIISVLGRDEPEWWRGELNGLSGLFPSNYVGPFVTSGKPAKANGTTKK). The protein was expressed in bacteria and purified with a Ni^{2+}-column followed by gel filtration. Sera were not pooled, and experiments reported here used the pre-production test bleed.

Guinea pig anti-Dynamin antisera were provided by D. Dickman; they were raised against a recombinant peptide conjugated to KLH (sequence: (C)-RPGGSLPPPMLPSRR).

Rabbit anti-EndoA polyclonal antisera were provided by D. Dickman; they were raised against a recombinant protein with a 6x-His N-terminal tag expressed in bacteria and purified with a Ni^{2+}-column (sequence: MHHHHHH-KEFLQPNPTARAKMAAVKGISKLSGQAKSNTYPQPEGLLAECMLTYGKKLGEDNSVFAQALVEFGEALKQMADVKYSLDDNIKQNFLEPLHHMQTKDLKEVMHHRKKLQGRRLDFDCKRRRQAKDDEIRGAEDKFGESLQLAQVGMFNLLENDTEHVSQLVTFAEALYDFHSQCADVLRGLQETLQEKRSEAESRPRNEFVPKTLLDLNLDGGGGGLNEDGTPSHISSSASPLPSPMRSPAKSMAVTPQRQQQPCCQALYDFE).

Immunostaining of *Drosophila* NMJs

For analyses of NMJ morphology and protein localization, flies were maintained at low density at 25°C. Wandering third instar larvae were dissected in Ca^{2+}-free HL3.1 saline (70 mM NaCl, 5 mM KCl, 10 mM $MgCl_2$, 10 mM $NaHCO_3$, 5 mM trehalose, 5 mM HEPES, 115 mM sucrose ***Feng et al., 2004***) and fixed for 20 min in HL3.1 containing 4% PFA. Fixed larvae were incubated in 'blocking solution' containing 3% BSA, 0.1% Triton X-100 in PBS for 30–60 min and incubated with primary antibody in blocking solution either overnight at 4°C or for 2 hr at room temperature. Samples were rinsed three times in a 'washing buffer' containing 0.1% Triton in PBS followed by three 10-min washes in washing buffer. Samples were incubated for 1 hr at room temperature with dye-conjugated secondary antibodies diluted to 1:250 in washing buffer, followed by washing as after primary antibody incubation. Larvae were mounted in Abberior Mount Liquid mounting medium. Primary antibodies used were rabbit anti-Nwk 970 (RRID:AB_2567353, knockout validated for immunostaining in ***Coyle et al., 2004***), guinea pig anti-Dynamin (gift from D. Dickman, validated for immunostaining by RNAi, ***Figure 2—figure supplement 1***), guinea pig anti-Dap160 (validated for immunostaining by RNAi, ***Figure 2—figure supplement 1***), rabbit anti-endophilin (gift from D. Dickman, validated for immunostaining by RNAi, ***Figure 2—figure supplement 1***), mouse anti-Dynamin (RRID:AB_397640, BD Biosciences Clone 41, validated for immunostaining by RNAi ***Kasprowicz et al., 2014***), mouse anti-BRP (RRID:AB_2314866, DSHB clone nc82, validated for immunostaining by RNAi ***Wagh et al., 2006***), rabbit anti-Pak (gift of N. Harden, mutant-validated for immunostaining, ***Harden et al., 1996***). Triple-labeling of Pak, FasII, and Brp was performed as follows: Samples were incubated with anti-Pak and anti-FasII primary antibodies overnight at 4°C, followed by washing, species specific secondary antibody incubation, and further washing using the same buffers and procedures as described above. Next, Brp was labeled using anti-Brp nc82; conjugated directly to Alexafluor-568, using a commercial antibody labeling kit (Thermo Fisher) for 4 hr at room temperature, followed by three 10-min washes.

NMJ image acquisition and processing

Confocal images of NMJs were acquired at room temperature with a Zeiss 880FAS microscope in SR mode, using a 63X (NA1.4) oil immersion objective and Zen Black software. All raw image stacks were processed in Zen Blue to construct Airyscan images using 3D Airyscan processing with automatic settings. Lateral and axial resolution were estimated to be ~175 and ~400 nm, respectively, by imaging Tetraspeck beads (Invitrogen) at 560 nm. To prepare images for analyses, we excluded regions that were obscured by axon bundles or contained Type 1s terminals.

To measure intensities in whole boutons, a 3D presynaptic mask was generated as follows. We produced a normalized sum image of Nwk, Dynamin, and Brp signals (except ***Figure 6***, which lacks Brp staining) by dividing each channel by its mean and summing the channels. Sum images were then gaussian filtered (sigma = 5 pixels for all experiments except ***Figure 9C–G***, where sigma = 4) and thresholded by intensity by a previously established algorithm (***Li and Tam, 1998***) (except ***Figure 9C–G***, which used Otsu thresholding ***Otsu, 1979***). The binary mask was eroded by 4 pixels (1 pixel for ***Figure 9C–G***). Mask settings were manually confirmed to accurately represent the 3D volume across images, and identical settings were used within an experiment. For all images, the background was subtracted using the rolling ball method with a radius of 50 pixels, and signal intensities were measured in 3D using a custom FIJI script (available at https://github.com/rodallab/nmj-measurement, copy archived at ***Rodallab, 2026***). For measurements of protein levels and polarization at the periactive zone, we used custom FIJI and Python scripts described in detail (***Del Signore et al., 2023***) and available at https://github.com/rodallab/paz-analysis, ***Rodallab, 2022***. First, maximum intensity projections were made of the upper half of NMJ terminals, to analyze a single plasma membrane surface. Second, a 2D mask of the total presynaptic area was generated by summing all channels in each image and then thresholded by intensity using a previously established algorithm (***Li and Tam, 1998***). Third, a periactive zone mesh composite image was created by subtracting the Brp signal from the sum of Nwk and Dyn signals, with the following exceptions: For ***Figure 6***, only the Nwk was used. For ***Figure 9L–N***, Brp and PAK signals were subtracted from FasII to create the composite mask. Fourth, periactive zone units were detected as local intensity minima and then expanded by the seeded region growing algorithm (via the IJ-Plugins Toolkit). The thresholds for minima detection were computed automatically and periactive zones detected at the edge of boutons (defined as having a mean Euclidean distance map score of less than 7.5 pixels) were excluded from analysis as these are

not planar (***Del Signore et al., 2023***). As above, settings were applied identically within an experiment. Image analyses settings were computed without manual user intervention, and data acquisition and analyses were not blinded. For representative images, brightness and contrast were linearly adjusted and applied identically to representative images of the same channel within an experiment.

Electrical stimulation of *Drosophila* NMJs

Control *white*^{1118} animals were dissected at room temperature in HL3.1 with 0 mM extracellular Ca^{2+}, and motor axons were cut close to the ventral ganglion. Prior to electrical stimulation, the tissue sample was washed three times with 1 ml of HL3.1 solution containing 2 mM Ca^{2+} and 7 mM glutamate (70 mM NaCl, 5 mM KCl, 10 mM $MgCl_2$, 10 mM $NaHCO_3$, 5 mM trehalose, 5 mM HEPES, 115 mM sucrose, 2 mM $CaCl_2$, 7 mM monosodium glutamate). The axon bundle innervating segment A3 was sucked into a pipette and 40 Hz stimulation was administered for 3 min (5 V for 0.5 ms per stimulus) at room temperature. The stimulus was administered through an A-M system 2100 stimulator using ADinstruments lab chart software. Stimulation was monitored by observing muscle contraction of the desired abdominal segment through the eyepiece. For stimulation experiments, muscles 6/7 and muscle 4 were imaged and analyzed together. As controls, comparisons were made to NMJs from the contralateral, unstimulated muscles. After stimulation, the preparation was stretched and fixed within 30 s with 4% PFA for 15 min, and samples were processed for immunohistochemistry as described above.

Statistics

Data are shown as mean ± SEM. For analyses of STED images of hippocampal synapses, the sample size is the number of analyzed synapses. For analyses of confocal images of hippocampal synapses, the sample size is the number of analyzed images. For analyses of *Drosophila* NMJs, the sample size is the number of analyzed NMJ terminals. Sample sizes and statistical tests are included in each figure legend. Significance is reported as *p < 0.05, **p < 0.01, or ***p < 0.001 and was assessed using parametric (*t*-test or one-way ANOVA) or non-parametric (Mann–Whitney *U* or Kruskal–Wallis) tests depending on whether assumptions of normality and homogeneity of variances were met (assessed using Shapiro or Levene's tests, respectively). Tukey–Kramer or Holm corrections for multiple testing were applied. In ***Figure 1***, ***Figure 1—figure supplement 1***, post hoc comparisons between all groups were performed, and only significance relative to the untreated condition is reported. For STED images, statistical analyses were performed on the peak values of the line profiles. Statistical analyses were performed in R. Sample sizes were determined based on previous studies.

Acknowledgements

We thank C Qiao, V Charles, G Handy, L Westhoff, A Silveira, and M Quiñones-Frías for technical support, and members of the Kaeser and Rodal laboratories for insightful discussions. We thank P De Camilli for anti-Dynamin-1, anti-PIPK1γ, and anti-AP-180 antibodies, D Dickman for anti-Dynamin and anti-EndoA antibodies, N Harden for anti-Pak antibodies, AMJM van den Maagdenberg for $Ca_V2.1$ floxed mice, T Schneider for $Ca_V2.3$ floxed mice, and Troy Littleton for brp mutant flies. This work was supported by grants from the NIH (R01MH113349 and R01NS083898 to PSK, R01NS116375 to AAR, T32007292 to KMDLG, S10 OD034223 for the Abberior Facility Line STED microscope, and K99NS129959 to JE-M), from the NSF (Brandeis Materials Research and Engineering Center NSF-DMR 2011846), and from Harvard Medical School (Harvard/MIT Joint Research Grant in Basic Neuroscience to PSK and AAR). JE-M was supported by an Alice and Joseph E Brooks postdoctoral fellowship from Harvard Medical School. We used fly stocks from the Bloomington *Drosophila* Stock Center (NIH P40OD018537) and antibodies from the Developmental Studies Hybridoma Bank, generated by the NICHD of the NIH. We acknowledge the Harvard Neurobiology Imaging Facility and Brandeis University Light Microscopy Core Facility Imaging Facility (RRID:SCR_025892).

Additional information

Funding

Funder	Grant reference number	Author
National Institutes of Health	R01MH113349	Pascal S Kaeser
National Institutes of Health	R01NS083898	Pascal S Kaeser
National Institutes of Health	R01NS116375	Avital A Rodal
National Institutes of Health	T32007292	Kevin M De León González
Harvard Medical School		Pascal S Kaeser Avital A Rodal
National Institutes of Health	S10 OD034223	Avital A Rodal
U.S. National Science Foundation	NSF-DMR 2011846	Steven J Del Signore Avital A Rodal
National Institutes of Health	K99NS129959	Javier Emperador-Melero

The funders had no role in study design, data collection, and interpretation, or the decision to submit the work for publication.

Author contributions

Javier Emperador-Melero, Conceptualization, Formal analysis, Funding acquisition, Investigation, Methodology, Writing – original draft, Writing – review and editing; Steven J Del Signore, Conceptualization, Formal analysis, Investigation, Methodology, Writing – original draft, Writing – review and editing; Kevin M De León González, Formal analysis, Investigation, Writing – review and editing; Pascal S Kaeser, Avital A Rodal, Conceptualization, Supervision, Funding acquisition, Writing – original draft, Writing – review and editing

Author ORCIDs

Javier Emperador-Melero https://orcid.org/0000-0002-1364-4935
Steven J Del Signore https://orcid.org/0000-0001-6007-9732
Kevin M De León González https://orcid.org/0000-0003-1315-7798
Pascal S Kaeser https://orcid.org/0000-0002-1558-1958
Avital A Rodal https://orcid.org/0000-0002-2051-8304

Ethics

Animal experiments were approved by the Harvard University Animal Care and Use Committee (protocol number IS00000049).

Peer review material

Reviewer #1 (Public review): https://doi.org/10.7554/eLife.107276.3.sa1
Reviewer #2 (Public review): https://doi.org/10.7554/eLife.107276.3.sa2
Reviewer #3 (Public review): https://doi.org/10.7554/eLife.107276.3.sa3
Author response https://doi.org/10.7554/eLife.107276.3.sa4

Additional files

Supplementary files

MDAR checklist

Data availability

Data points generated for this study are included in the figures. Raw numerical data used to generate all figures are available at https://doi.org/10.5281/zenodo.20071165. Images, code, and raw data for *Drosophila* experiments are available at https://doi.org/10.5281/zenodo.17202731.

The following datasets were generated:

Author(s)	Year	Dataset title	Dataset URL	Database and Identifier
Emperador-Melero J	2026	Data table for Emperador-Melero, Del Signore et al; "Deployment of endocytic machinery to periactive zones of nerve terminals is independent of active zone assembly and evoked release"	https://doi.org/10.5281/zenodo.20071165	Zenodo, 10.5281/zenodo.20071165
Emperador Melero J, Del Signore S, De Leon Gonzalez K, Kaeser P, Rodal A	2025	Deployment of endocytic machinery to periactive zones of nerve terminals is independent of active zone assembly and evoked release: Drosophila Data	https://doi.org/10.5281/zenodo.17202731	Zenodo, 10.5281/zenodo.17202731

References

Acuna C, Liu X, Südhof TC. 2016. How to make an active zone: unexpected universal functional redundancy between RIMs and RIM-BPs. *Neuron* **91**:792–807. DOI: https://doi.org/10.1016/j.neuron.2016.07.042, PMID: 27537484

Akbergenova Y, Cunningham KL, Zhang YV, Weiss S, Littleton JT. 2018. Characterization of developmental and molecular factors underlying release heterogeneity at *Drosophila* synapses. *eLife* **7**:e38268. DOI: https://doi.org/10.7554/eLife.38268, PMID: 29989549

Akbergenova Y, Matthias J, Makeyeva S, Littleton JT. 2025. Active zone maturation controls presynaptic output and release mode and is regulated by neuronal activity. *The Journal of Neuroscience* **45**:e1143252025. DOI: https://doi.org/10.1523/JNEUROSCI.1143-25.2025, PMID: 41087171

Anantharam A, Bittner MA, Aikman RL, Stuenkel EL, Schmid SL, Axelrod D, Holz RW. 2011. A new role for the dynamin GTPase in the regulation of fusion pore expansion. *Molecular Biology of the Cell* **22**:1907–1918. DOI: https://doi.org/10.1091/mbc.E11-02-0101, PMID: 21460182

Aravamudan B, Fergestad T, Davis WS, Rodesch CK, Broadie K. 1999. *Drosophila* UNC-13 is essential for synaptic transmission. *Nature Neuroscience* **2**:965–971. DOI: https://doi.org/10.1038/14764, PMID: 10526334

Bademosi AT, Decet M, Kuenen S, Calatayud C, Swerts J, Gallego SF, Schoovaerts N, Karamanou S, Louros N, Martin E, Sibarita JB, Vints K, Gounko NV, Meunier FA, Economou A, Versées W, Rousseau F, Schymkowitz J, Soukup SF, Verstreken P. 2023. EndophilinA-dependent coupling between activity-induced calcium influx and synaptic autophagy is disrupted by a Parkinson-risk mutation. *Neuron* **111**:1402–1422. DOI: https://doi.org/10.1016/j.neuron.2023.02.001, PMID: 36827984

Bai J, Tucker WC, Chapman ER. 2004. PIP2 increases the speed of response of synaptotagmin and steers its membrane-penetration activity toward the plasma membrane. *Nature Structural & Molecular Biology* **11**:36–44. DOI: https://doi.org/10.1038/nsmb709, PMID: 14718921

Bai J, Hu Z, Dittman JS, Pym ECG, Kaplan JM. 2010. Endophilin functions as a membrane-bending molecule and is delivered to endocytic zones by exocytosis. *Cell* **143**:430–441. DOI: https://doi.org/10.1016/j.cell.2010.09.024, PMID: 21029864

Bailey CH, Chen M, Keller F, Kandel ER. 1992. Serotonin-mediated endocytosis of apCAM: an early step of learning-related synaptic growth in Aplysia. *Science* **256**:645–649. DOI: https://doi.org/10.1126/science.1585177, PMID: 1585177

Biederer T, Kaeser PS, Blanpied TA. 2017. Transcellular nanoalignment of synaptic function. *Neuron* **96**:680–696. DOI: https://doi.org/10.1016/j.neuron.2017.10.006, PMID: 29096080

Blanchette CR, Scalera AL, Harris KP, Zhao Z, Dresselhaus EC, Koles K, Yeh A, Apiki JK, Stewart BA, Rodal AA. 2022. Local regulation of extracellular vesicle traffic by the synaptic endocytic machinery. *Journal of Cell Biology* **221**:e202112094. DOI: https://doi.org/10.1083/JCB.202112094/213086, PMID: 35320349

Bloom O, Evergren E, Tomilin N, Kjaerulff O, Löw P, Brodin L, Pieribone VA, Greengard P, Shupliakov O. 2003. Colocalization of synapsin and actin during synaptic vesicle recycling. *The Journal of Cell Biology* **161**:737–747. DOI: https://doi.org/10.1083/jcb.200212140, PMID: 12756235

Böhme MA, Beis C, Reddy-Alla S, Reynolds E, Mampell MM, Grasskamp AT, Lützkendorf J, Bergeron DD, Driller JH, Babikir H, Göttfert F, Robinson IM, O'Kane CJ, Hell SW, Wahl MC, Stelzl U, Loll B, Walter AM, Sigrist SJ. 2016. Active zone scaffolds differentially accumulate Unc13 isoforms to tune Ca(2+) channel-vesicle coupling. *Nature Neuroscience* **19**:1311–1320. DOI: https://doi.org/10.1038/nn.4364, PMID: 27526206

Bolz S, Kaempf N, Puchkov D, Krauss M, Russo G, Soykan T, Schmied C, Lehmann M, Müller R, Schultz C, Perrais D, Maritzen T, Haucke V. 2023. Synaptotagmin 1-triggered lipid signaling facilitates coupling of exo- and endocytosis. *Neuron* **111**:3765–3774.. DOI: https://doi.org/10.1016/j.neuron.2023.08.016, PMID: 37738980

Brenig J, de Boor S, Knyphausen P, Kuhlmann N, Wroblowski S, Baldus L, Scislowski L, Artz O, Trauschies P, Baumann U, Neundorf I, Lammers M. 2015. Structural and biochemical basis for the inhibitory effect of liprin-α3 on mouse diaphanous 1 (mDia1) function. *The Journal of Biological Chemistry* **290**:14314–14327. DOI: https://doi.org/10.1074/jbc.M114.621946, PMID: 25911102

Cao Y-Q, Piedras-Rentería ES, Smith GB, Chen G, Harata NC, Tsien RW. 2004. Presynaptic Ca2+ channels compete for channel type-preferring slots in altered neurotransmission arising from Ca2+ channelopathy. *Neuron* **43**:387–400. DOI: https://doi.org/10.1016/j.neuron.2004.07.014, PMID: 15294146

Chia PH, Patel MR, Shen K. 2012. NAB-1 instructs synapse assembly by linking adhesion molecules and F-actin to active zone proteins. *Nature Neuroscience* **15**:234–242. DOI: https://doi.org/10.1038/nn.2991, PMID: 22231427

Chin M, Kaeser PS. 2024. The intracellular C-terminus confers compartment-specific targeting of voltage-gated calcium channels. *Cell Reports* **43**:114428. DOI: https://doi.org/10.1016/j.celrep.2024.114428, PMID: 38996073

Cocucci E, Gaudin R, Kirchhausen T. 2014. Dynamin recruitment and membrane scission at the neck of a clathrin-coated pit. *Molecular Biology of the Cell* **25**:3595–3609. DOI: https://doi.org/10.1091/mbc.E14-07-1240, PMID: 25232009

Coyle IP, Koh YH, Lee WCM, Slind J, Fergestad T, Littleton JT, Ganetzky B. 2004. Nervous wreck, an SH3 adaptor protein that interacts with Wsp, regulates synaptic growth in *Drosophila*. *Neuron* **41**:521–534. DOI: https://doi.org/10.1016/s0896-6273(04)00016-9, PMID: 14980202

Cunningham KL, Sauvola CW, Tavana S, Littleton JT. 2022. Regulation of presynaptic Ca^{2+} channel abundance at active zones through a balance of delivery and turnover. *eLife* **11**:e78648. DOI: https://doi.org/10.7554/eLife.78648, PMID: 35833625

de Jong APH, Roggero CM, Ho M-R, Wong MY, Brautigam CA, Rizo J, Kaeser PS. 2018. RIM C2B domains target presynaptic active zone functions to PIP2-containing membranes. *Neuron* **98**:335–349. DOI: https://doi.org/10.1016/j.neuron.2018.03.011, PMID: 29606581

Del Signore SJ, Kelley CF, Messelaar EM, Lemos T, Marchan MF, Ermanoska B, Mund M, Fai TG, Kaksonen M, Rodal AA. 2021. An autoinhibitory clamp of actin assembly constrains and directs synaptic endocytosis. *eLife* **10**:e69597. DOI: https://doi.org/10.7554/eLife.69597, PMID: 34324418

Del Signore SJ, Mitzner MG, Silveira AM, Fai TG, Rodal AA. 2023. An approach for quantitative mapping of synaptic periactive zone architecture and organization. *Molecular Biology of the Cell* **34**:ar51. DOI: https://doi.org/10.1091/mbc.E22-08-0372, PMID: 36542486

Di Paolo G, Sankaranarayanan S, Wenk MR, Daniell L, Perucco E, Caldarone BJ, Flavell R, Picciotto MR, Ryan TA, Cremona O, De Camilli P. 2002. Decreased synaptic vesicle recycling efficiency and cognitive deficits in amphiphysin 1 knockout mice. *Neuron* **33**:789–804. DOI: https://doi.org/10.1016/s0896-6273(02)00601-3, PMID: 11879655

Di Paolo G, Moskowitz HS, Gipson K, Wenk MR, Voronov S, Obayashi M, Flavell R, Fitzsimonds RM, Ryan TA, De Camilli P. 2004. Impaired PtdIns(4,5)P2 synthesis in nerve terminals produces defects in synaptic vesicle trafficking. *Nature* **431**:415–422. DOI: https://doi.org/10.1038/nature02896, PMID: 15386003

Emperador-Melero J, Kaeser PS. 2020. Assembly of the presynaptic active zone. *Current Opinion in Neurobiology* **63**:95–103. DOI: https://doi.org/10.1016/j.conb.2020.03.008, PMID: 32403081

Emperador-Melero J, de Nola G, Kaeser PS. 2021a. Intact synapse structure and function after combined knockout of PTPδ, PTPσ, and LAR. *eLife* **10**:e66638. DOI: https://doi.org/10.7554/eLife.66638, PMID: 33656439

Emperador-Melero J, Wong MY, Wang SSH, de Nola G, Nyitrai H, Kirchhausen T, Kaeser PS. 2021b. PKC-phosphorylation of Liprin-α3 triggers phase separation and controls presynaptic active zone structure. *Nature Communications* **12**:3057. DOI: https://doi.org/10.1038/s41467-021-23116-w, PMID: 34031393

Emperador-Melero J, Andersen JW, Metzbower SR, Levy AD, Dharmasri PA, de Nola G, Blanpied TA, Kaeser PS. 2024. Distinct active zone protein machineries mediate Ca^{2+} channel clustering and vesicle priming at hippocampal synapses. *Nature Neuroscience* **27**:1680–1694. DOI: https://doi.org/10.1038/s41593-024-01720-5, PMID: 39160372

Estes PS, Roos J, van der Bliek A, Kelly RB, Krishnan KS, Ramaswami M. 1996. Traffic of dynamin within individual *Drosophila* synaptic boutons relative to compartment-specific markers. *The Journal of Neuroscience* **16**:5443–5456. DOI: https://doi.org/10.1523/JNEUROSCI.16-17-05443.1996, PMID: 8757257

Feng Y, Ueda A, Wu CF. 2004. A modified minimal hemolymph-like solution, hl3.1, for physiological recordings at the neuromuscular junctions of normal and mutant *Drosophila* larvae. *Journal of Neurogenetics* **18**:377–402. DOI: https://doi.org/10.1080/01677060490894522, PMID: 15763995

Ferguson SM, Brasnjo G, Hayashi M, Wölfel M, Collesi C, Giovedi S, Raimondi A, Gong L-W, Ariel P, Paradise S, O'toole E, Flavell R, Cremona O, Miesenböck G, Ryan TA, De Camilli P. 2007. A selective activity-dependent requirement for dynamin 1 in synaptic vesicle endocytosis. *Science* **316**:570–574. DOI: https://doi.org/10.1126/science.1140621, PMID: 17463283

Fouquet W, Owald D, Wichmann C, Mertel S, Depner H, Dyba M, Hallermann S, Kittel RJ, Eimer S, Sigrist SJ. 2009. Maturation of active zone assembly by *Drosophila* Bruchpilot. *The Journal of Cell Biology* **186**:129–145. DOI: https://doi.org/10.1083/jcb.200812150, PMID: 19596851

Fu Y, Huang ZJ. 2010. Differential dynamics and activity-dependent regulation of alpha- and beta-neurexins at developing GABAergic synapses. *PNAS* **107**:22699–22704. DOI: https://doi.org/10.1073/pnas.1011233108, PMID: 21149722

Ganguly A, Sharma R, Boyer NP, Wernert F, Phan S, Boassa D, Parra L, Das U, Caillol G, Han X, Yates JR III, Ellisman MH, Leterrier C, Roy S. 2021. Clathrin packets move in slow axonal transport and deliver functional payloads to synapses. *Neuron* **109**:2884–2901. DOI: https://doi.org/10.1016/j.neuron.2021.08.016, PMID: 34534453

Gerth F, Jäpel M, Pechstein A, Kochlamazashvili G, Lehmann M, Puchkov D, Onofri F, Benfenati F, Nikonenko AG, Fredrich K, Shupliakov O, Maritzen T, Freund C, Haucke V. 2017. Intersectin associates with synapsin and regulates its nanoscale localization and function. *PNAS* **114**:12057–12062. DOI: https://doi.org/10.1073/pnas.1715341114, PMID: 29078407

Gimber N, Tadeus G, Maritzen T, Schmoranzer J, Haucke V. 2015. Diffusional spread and confinement of newly exocytosed synaptic vesicle proteins. *Nature Communications* **6**:8392. DOI: https://doi.org/10.1038/ncomms9392, PMID: 26399746

Graf ER, Daniels RW, Burgess RW, Schwarz TL, DiAntonio A. 2009. Rab3 dynamically controls protein composition at active zones. *Neuron* **64**:663–677. DOI: https://doi.org/10.1016/j.neuron.2009.11.002, PMID: 20005823

Graf ER, Valakh V, Wright CM, Wu C, Liu Z, Zhang YQ, DiAntonio A. 2012. RIM promotes calcium channel accumulation at active zones of the *Drosophila* neuromuscular junction. *The Journal of Neuroscience* **32**:16586–16596. DOI: https://doi.org/10.1523/JNEUROSCI.0965-12.2012, PMID: 23175814

Harden N, Lee J, Loh HY, Ong YM, Tan I, Leung T, Manser E, Lim L. 1996. A *Drosophila* homolog of the Rac- and Cdc42-activated serine/threonine kinase PAK is a potential focal adhesion and focal complex protein that colocalizes with dynamic actin structures. *Molecular and Cellular Biology* **16**:1896–1908. DOI: https://doi.org/10.1128/MCB.16.5.1896, PMID: 8628256

Harris KP, Littleton JT. 2015. Transmission, development, and plasticity of synapses. *Genetics* **201**:345–375. DOI: https://doi.org/10.1534/genetics.115.176529, PMID: 26447126

Haucke V, De Camilli P. 1999. AP-2 recruitment to synaptotagmin stimulated by tyrosine-based endocytic motifs. *Science* **285**:1268–1271. DOI: https://doi.org/10.1126/science.285.5431.1268, PMID: 10455054

Haucke V, Neher E, Sigrist SJ. 2011. Protein scaffolds in the coupling of synaptic exocytosis and endocytosis. *Nature Reviews. Neuroscience* **12**:127–138. DOI: https://doi.org/10.1038/nrn2948, PMID: 21304549

Held RG, Liu C, Ma K, Ramsey AM, Tarr TB, De Nola G, Wang SSH, Wang J, van den Maagdenberg A, Schneider T, Sun J, Blanpied TA, Kaeser PS. 2020. Synapse and active zone assembly in the absence of presynaptic Ca2+ channels and Ca2+ entry. *Neuron* **107**:667–683. DOI: https://doi.org/10.1016/j.neuron.2020.05.032, PMID: 32616470

Hua Y, Sinha R, Thiel CS, Schmidt R, Hüve J, Martens H, Hell SW, Egner A, Klingauf J. 2011. A readily retrievable pool of synaptic vesicles. *Nature Neuroscience* **14**:833–839. DOI: https://doi.org/10.1038/nn.2838, PMID: 21666673

Imoto Y, Raychaudhuri S, Ma Y, Fenske P, Sandoval E, Itoh K, Blumrich EM, Matsubayashi HT, Mamer L, Zarebidaki F, Söhl-Kielczynski B, Trimbuch T, Nayak S, Iwasa JH, Liu J, Wu B, Ha T, Inoue T, Jorgensen EM, Cousin MA, et al. 2022. Dynamin is primed at endocytic sites for ultrafast endocytosis. *Neuron* **110**:2815–2835. DOI: https://doi.org/10.1016/j.neuron.2022.06.010, PMID: 35809574

Imoto Y, Xue J, Luo L, Raychaudhuri S, Itoh K, Ma Y, Craft GE, Kwan AH, Ogunmowo TH, Ho A, Mackay JP, Ha T, Watanabe S, Robinson PJ. 2024. Dynamin 1xA interacts with Endophilin A1 via its spliced long C-terminus for ultrafast endocytosis. *The EMBO Journal* **43**:3327–3357. DOI: https://doi.org/10.1038/s44318-024-00145-x, PMID: 38907032

Jäpel M, Gerth F, Sakaba T, Bacetic J, Yao L, Koo SJ, Maritzen T, Freund C, Haucke V. 2020. Intersectin-mediated clearance of SNARE complexes is required for fast neurotransmission. *Cell Reports* **30**:409–420. DOI: https://doi.org/10.1016/j.celrep.2019.12.035, PMID: 31940485

Jenett A, Rubin GM, Ngo TTB, Shepherd D, Murphy C, Dionne H, Pfeiffer BD, Cavallaro A, Hall D, Jeter J, Iyer N, Fetter D, Hausenfluck JH, Peng H, Trautman ET, Svirskas RR, Myers EW, Iwinski ZR, Aso Y, DePasquale GM, et al. 2012. A GAL4-driver line resource for *Drosophila* neurobiology. *Cell Reports* **2**:991–1001. DOI: https://doi.org/10.1016/j.celrep.2012.09.011, PMID: 23063364

Jiang A, Kudo K, Gormal RS, Ellis S, Guo S, Wallis TP, Longfield SF, Robinson PJ, Johnson ME, Joensuu M, Meunier FA. 2024. Dynamin1 long- and short-tail isoforms exploit distinct recruitment and spatial patterns to form endocytic nanoclusters. *Nature Communications* **15**:4060. DOI: https://doi.org/10.1038/s41467-024-47677-8, PMID: 38744819

Jiao W, Shupliakov A, Shupliakov O. 2010. A semi-correlative technique for the subcellular localization of proteins in *Drosophila* synapses. *Journal of Neuroscience Methods* **185**:273–279. DOI: https://doi.org/10.1016/j.jneumeth.2009.10.010, PMID: 19850080

Jorgensen EM, Hartwieg E, Schuske K, Nonet ML, Jin Y, Horvitz HR. 1995. Defective recycling of synaptic vesicles in synaptotagmin mutants of *Caenorhabditis elegans*. *Nature* **378**:196–199. DOI: https://doi.org/10.1038/378196a0, PMID: 7477324

Kaeser PS, Kwon H-B, Chiu CQ, Deng L, Castillo PE, Südhof TC. 2008. RIM1alpha and RIM1beta are synthesized from distinct promoters of the RIM1 gene to mediate differential but overlapping synaptic functions. *The Journal of Neuroscience* **28**:13435–13447. DOI: https://doi.org/10.1523/JNEUROSCI.3235-08.2008, PMID: 19074017

Kaeser PS, Deng L, Chávez AE, Liu X, Castillo PE, Südhof TC. 2009. ELKS2alpha/CAST deletion selectively increases neurotransmitter release at inhibitory synapses. *Neuron* **64**:227–239. DOI: https://doi.org/10.1016/j.neuron.2009.09.019, PMID: 19874790

Kaeser PS, Deng L, Wang Y, Dulubova I, Liu X, Rizo J, Südhof TC. 2011. RIM proteins tether Ca2+ channels to presynaptic active zones via a direct PDZ-domain interaction. *Cell* **144**:282–295. DOI: https://doi.org/10.1016/j.cell.2010.12.029, PMID: 21241895

Kaeser PS, Regehr WG. 2014. Molecular mechanisms for synchronous, asynchronous, and spontaneous neurotransmitter release. *Annual Review of Physiology* **76**:333–363. DOI: https://doi.org/10.1146/annurev-physiol-021113-170338, PMID: 24274737

Kaeserlab. 2020. 3DSIM_Analysis_CL. d4278e8. Github. https://github.com/kaeserlab/3DSIM_Analysis_CL

Kaksonen M, Roux A. 2018. Mechanisms of clathrin-mediated endocytosis. *Nature Reviews. Molecular Cell Biology* **19**:313–326. DOI: https://doi.org/10.1038/nrm.2017.132, PMID: 29410531

Kasprowicz J, Kuenen S, Swerts J, Miskiewicz K, Verstreken P. 2014. Dynamin photoinactivation blocks Clathrin and α-adaptin recruitment and induces bulk membrane retrieval. *The Journal of Cell Biology* **204**:1141–1156. DOI: https://doi.org/10.1083/jcb.201310090, PMID: 24662566

Kaufmann N, DeProto J, Ranjan R, Wan H, Van Vactor D. 2002. *Drosophila* liprin-alpha and the receptor phosphatase Dlar control synapse morphogenesis. *Neuron* **34**:27–38. DOI: https://doi.org/10.1016/s0896-6273(02)00643-8, PMID: 11931739

Kawasaki F, Hazen M, Ordway RW. 2000. Fast synaptic fatigue in shibire mutants reveals a rapid requirement for dynamin in synaptic vesicle membrane trafficking. *Nature Neuroscience* **3**:859–860. DOI: https://doi.org/10.1038/78753, PMID: 10966613

Kittel RJ, Wichmann C, Rasse TM, Fouquet W, Schmidt M, Schmid A, Wagh DA, Pawlu C, Kellner RR, Willig KI, Hell SW, Buchner E, Heckmann M, Sigrist SJ. 2006. Bruchpilot promotes active zone assembly, Ca2+ channel clustering, and vesicle release. *Science* **312**:1051–1054. DOI: https://doi.org/10.1126/science.1126308, PMID: 16614170

Koh T-W, Korolchuk VI, Wairkar YP, Jiao W, Evergren E, Pan H, Zhou Y, Venken KJT, Shupliakov O, Robinson IM, O'Kane CJ, Bellen HJ. 2007. Eps15 and Dap160 control synaptic vesicle membrane retrieval and synapse development. *The Journal of Cell Biology* **178**:309–322. DOI: https://doi.org/10.1083/jcb.200701030, PMID: 17620409

Koo SJ, Kochlamazashvili G, Rost B, Puchkov D, Gimber N, Lehmann M, Tadeus G, Schmoranzer J, Rosenmund C, Haucke V, Maritzen T. 2015. Vesicular synaptobrevin/VAMP2 levels guarded by AP180 control efficient neurotransmission. *Neuron* **88**:330–344. DOI: https://doi.org/10.1016/j.neuron.2015.08.034, PMID: 26412491

Li CH, Tam PKS. 1998. An iterative algorithm for minimum cross entropy thresholding. *Pattern Recognition Letters* **19**:771–776. DOI: https://doi.org/10.1016/S0167-8655(98)00057-9

Li TN, Chen YJ, Lu TY, Wang YT, Lin HC, Yao CK. 2020. A positive feedback loop between Flower and PI(4,5)P_2 at periactive zones controls bulk endocytosis in Drosophila. *eLife* **9**:e60125. DOI: https://doi.org/10.7554/eLife.60125, PMID: 33300871

Liu KSY, Siebert M, Mertel S, Knoche E, Wegener S, Wichmann C, Matkovic T, Muhammad K, Depner H, Mettke C, Bückers J, Hell SW, Müller M, Davis GW, Schmitz D, Sigrist SJ. 2011. RIM-binding protein, a central part of the active zone, is essential for neurotransmitter release. *Science* **334**:1565–1569. DOI: https://doi.org/10.1126/science.1212991, PMID: 22174254

Liu C, Bickford LS, Held RG, Nyitrai H, Südhof TC, Kaeser PS. 2014. The active zone protein family ELKS supports Ca2+ influx at nerve terminals of inhibitory hippocampal neurons. *The Journal of Neuroscience* **34**:12289–12303. DOI: https://doi.org/10.1523/JNEUROSCI.0999-14.2014, PMID: 25209271

Liu C, Kershberg L, Wang J, Schneeberger S, Kaeser PS. 2018. Dopamine secretion is mediated by sparse active zone-like release sites. *Cell* **172**:706–718. DOI: https://doi.org/10.1016/j.cell.2018.01.008, PMID: 29398114

Marcó de la Cruz B, Campos J, Molinaro A, Xie X, Jin G, Wei Z, Acuna C, Sterky FH. 2024. Liprin-α proteins are master regulators of human presynapse assembly. *Nature Neuroscience* **27**:629–642. DOI: https://doi.org/10.1038/s41593-024-01592-9, PMID: 38472649

McDonald NA, Fetter RD, Shen K. 2020. Assembly of synaptic active zones requires phase separation of scaffold molecules. *Nature* **588**:454–458. DOI: https://doi.org/10.1038/s41586-020-2942-0, PMID: 33208945

Milosevic I, Giovedi S, Lou X, Raimondi A, Collesi C, Shen H, Paradise S, O'Toole E, Ferguson S, Cremona O, De Camilli P. 2011. Recruitment of endophilin to clathrin-coated pit necks is required for efficient vesicle uncoating after fission. *Neuron* **72**:587–601. DOI: https://doi.org/10.1016/j.neuron.2011.08.029, PMID: 22099461

Milovanovic D, Wu Y, Bian X, De Camilli P. 2018. A liquid phase of synapsin and lipid vesicles. *Science* **361**:604–607. DOI: https://doi.org/10.1126/science.aat5671, PMID: 29976799

Moro A, van Nifterick A, Toonen RF, Verhage M. 2021. Dynamin controls neuropeptide secretion by organizing dense-core vesicle fusion sites. *Science Advances* **7**:eabf0659. DOI: https://doi.org/10.1126/sciadv.abf0659, PMID: 34020952

Mueller VJ, Wienisch M, Nehring RB, Klingauf J. 2004. Monitoring clathrin-mediated endocytosis during synaptic activity. *The Journal of Neuroscience* **24**:2004–2012. DOI: https://doi.org/10.1523/JNEUROSCI.4080-03.2004, PMID: 14985443

Nyitrai H, Wang SSH, Kaeser PS. 2020. ELKS1 captures Rab6-marked vesicular cargo in presynaptic nerve terminals. *Cell Reports* **31**:107712. DOI: https://doi.org/10.1016/j.celrep.2020.107712, PMID: 32521280

Ogunmowo TH, Jing H, Raychaudhuri S, Kusick GF, Imoto Y, Li S, Itoh K, Ma Y, Jafri H, Dalva MB, Chapman ER, Ha T, Watanabe S, Liu J. 2023. Membrane compression by synaptic vesicle exocytosis triggers ultrafast endocytosis. *Nature Communications* **14**:2888. DOI: https://doi.org/10.1038/s41467-023-38595-2, PMID: 37210439

Otsu N. 1979. A threshold selection method from gray-level histograms. *IEEE Transactions on Systems, Man, and Cybernetics* **9**:62–66. DOI: https://doi.org/10.1109/TSMC.1979.4310076

Owald D, Fouquet W, Schmidt M, Wichmann C, Mertel S, Depner H, Christiansen F, Zube C, Quentin C, Körner J, Urlaub H, Mechtler K, Sigrist SJ. 2010. A Syd-1 homologue regulates pre- and postsynaptic maturation in *Drosophila*. *The Journal of Cell Biology* **188**:565–579. DOI: https://doi.org/10.1083/jcb.200908055, PMID: 20176924

Peled ES, Isacoff EY. 2011. Optical quantal analysis of synaptic transmission in wild-type and rab3-mutant *Drosophila* motor axons. *Nature Neuroscience* **14**:519–526. DOI: https://doi.org/10.1038/nn.2767, PMID: 21378971

Pereverzev A, Mikhna M, Vajna R, Gissel C, Henry M, Weiergräber M, Hescheler J, Smyth N, Schneider T. 2002. Disturbances in glucose-tolerance, insulin-release, and stress-induced hyperglycemia upon disruption of the Ca(v)2.3 (alpha 1E) subunit of voltage-gated Ca(2+) channels. *Molecular Endocrinology* **16**:884–895. DOI: https://doi.org/10.1210/mend.16.4.0801, PMID: 11923483

Perez de Arce K, Schrod N, Metzbower SWR, Allgeyer E, Kong GKW, Tang AH, Krupp AJ, Stein V, Liu X, Bewersdorf J, Blanpied TA, Lucić V, Biederer T. 2015. Topographic mapping of the synaptic cleft into adhesive nanodomains. *Neuron* **88**:1165–1172. DOI: https://doi.org/10.1016/j.neuron.2015.11.011, PMID: 26687224

Poskanzer KE, Fetter RD, Davis GW. 2006. Discrete residues in the c(2)b domain of synaptotagmin I independently specify endocytic rate and synaptic vesicle size. *Neuron* **50**:49–62. DOI: https://doi.org/10.1016/j.neuron.2006.02.021, PMID: 16600855

Raimondi A, Ferguson SM, Lou X, Armbruster M, Paradise S, Giovedi S, Messa M, Kono N, Takasaki J, Cappello V, O'Toole E, Ryan TA, De Camilli P. 2011. Overlapping role of dynamin isoforms in synaptic vesicle endocytosis. *Neuron* **70**:1100–1114. DOI: https://doi.org/10.1016/j.neuron.2011.04.031, PMID: 21689597

Rao Y, Ma Q, Vahedi-Faridi A, Sundborger A, Pechstein A, Puchkov D, Luo L, Shupliakov O, Saenger W, Haucke V. 2010. Molecular basis for SH3 domain regulation of F-BAR-mediated membrane deformation. *PNAS* **107**:8213–8218. DOI: https://doi.org/10.1073/pnas.1003478107, PMID: 20404169

Reshetniak S, Ußling J-E, Perego E, Rammner B, Schikorski T, Fornasiero EF, Truckenbrodt S, Köster S, Rizzoli SO. 2020. A comparative analysis of the mobility of 45 proteins in the synaptic bouton. *The EMBO Journal* **39**:e104596. DOI: https://doi.org/10.15252/embj.2020104596, PMID: 32627850

Rodal AA, Motola-Barnes RN, Littleton JT. 2008. Nervous wreck and Cdc42 cooperate to regulate endocytic actin assembly during synaptic growth. *The Journal of Neuroscience* **28**:8316–8325. DOI: https://doi.org/10.1523/JNEUROSCI.2304-08.2008, PMID: 18701694

Rodallab. 2022. Paz-analysis. 93478cf. Github. https://github.com/rodallab/paz-analysis

Rodallab. 2026. Nmj-measurement. swh:1:rev:c25ff74ccd0c20bd917189eb4f224d779859cd7f. Software Heritage. https://archive.softwareheritage.org/swh:1:dir:60ce5027745690e22820c102430922bca49a7f33;origin=https://github.com/rodallab/nmj-measurement;visit=swh:1:snp:5d3703a23460e9bfb240e575a483d7d906da27fb;anchor=swh:1:rev:c25ff74ccd0c20bd917189eb4f224d779859cd7f

Roos J, Kelly RB. 1999. The endocytic machinery in nerve terminals surrounds sites of exocytosis. *Current Biology* **9**:1411–1414. DOI: https://doi.org/10.1016/s0960-9822(00)80087-1, PMID: 10607569

Saheki Y, De Camilli P. 2012. Synaptic vesicle endocytosis. *Cold Spring Harbor Perspectives in Biology* **4**:a005645. DOI: https://doi.org/10.1101/cshperspect.a005645, PMID: 22763746

Samasilp P, Chan SA, Smith C. 2012. Activity-dependent fusion pore expansion regulated by a calcineurin-dependent dynamin-syndapin pathway in mouse adrenal chromaffin cells. *The Journal of Neuroscience* **32**:10438–10447. DOI: https://doi.org/10.1523/JNEUROSCI.1299-12.2012, PMID: 22836276

Santos TC, Wierda K, Broeke JH, Toonen RF, Verhage M. 2017. Early golgi abnormalities and neurodegeneration upon loss of presynaptic proteins munc18-1, syntaxin-1, or SNAP-25. *The Journal of Neuroscience* **37**:4525–4539. DOI: https://doi.org/10.1523/JNEUROSCI.3352-16.2017, PMID: 28348137

Sclip A, Südhof TC. 2020. LAR receptor phospho-tyrosine phosphatases regulate NMDA-receptor responses. *eLife* **9**:eLife . DOI: https://doi.org/10.7554/eLife.53406, PMID: 31985401

Sclip A, Südhof TC. 2023. Combinatorial expression of neurexins and LAR-type phosphotyrosine phosphatase receptors instructs assembly of a cerebellar circuit. *Nature Communications* **14**:4976. DOI: https://doi.org/10.1038/s41467-023-40526-0, PMID: 37591863

Soukup SF, Verstreken P. 2017. EndoA/Endophilin-A creates docking stations for autophagic proteins at synapses. *Autophagy* **13**:971–972. DOI: https://doi.org/10.1080/15548627.2017.1286440, PMID: 28282269

Stanishneva-Konovalova TB, Kelley CF, Eskin TL, Messelaar EM, Wasserman SA, Sokolova OS, Rodal AA. 2016. Coordinated autoinhibition of F-BAR domain membrane binding and WASp activation by Nervous Wreck. *PNAS* **113**:E5552–E5561. DOI: https://doi.org/10.1073/pnas.1524412113, PMID: 27601635

Südhof TC. 2012. The presynaptic active zone. *Neuron* **75**:11–25. DOI: https://doi.org/10.1016/j.neuron.2012.06.012, PMID: 22794257

Sweeney ST, Broadie K, Keane J, Niemann H, O'Kane CJ. 1995. Targeted expression of tetanus toxin light chain in *Drosophila* specifically eliminates synaptic transmission and causes behavioral defects. *Neuron* **14**:341–351. DOI: https://doi.org/10.1016/0896-6273(95)90290-2, PMID: 7857643

Tan C, Wang SSH, de Nola G, Kaeser PS. 2022. Rebuilding essential active zone functions within a synapse. *Neuron* **110**:1498–1515. DOI: https://doi.org/10.1016/j.neuron.2022.01.026, PMID: 35176221

Tang AH, Chen H, Li TP, Metzbower SR, MacGillavry HD, Blanpied TA. 2016. A trans-synaptic nanocolumn aligns neurotransmitter release to receptors. *Nature* **536**:210–214. DOI: https://doi.org/10.1038/nature19058, PMID: 27462810

Taylor MJ, Perrais D, Merrifield CJ. 2011. A high precision survey of the molecular dynamics of mammalian clathrin-mediated endocytosis. *PLOS Biology* **9**:e1000604. DOI: https://doi.org/10.1371/journal.pbio.1000604, PMID: 21445324

Terry-Lorenzo RT, Torres VI, Wagh D, Galaz J, Swanson SK, Florens L, Washburn MP, Waites CL, Gundelfinger ED, Reimer RJ, Garner CC. 2016. Trio, a rho family GEF, interacts with the presynaptic active zone proteins piccolo and bassoon. *PLOS ONE* **11**:e0167535. DOI: https://doi.org/10.1371/journal.pone.0167535, PMID: 27907191

Thivaios S, Schwenk J, Brechet A, Boudkkazi S, Sethumadhavan N, Henneken P, Miura E, Hayashi A, Kocylowski MK, Haupt A, Kaminski D, Schreiner D, van den Broucke JB, Kulik A, Schulte U, Sterky FH, Yuzaki M, Scheiffele P, Fakler B. 2024. Ternary neurexin-T178-PTPR complexes represent a presynaptic core-module of neuronal synapse organization. *bioRxiv*. DOI: https://doi.org/10.1101/2024.07.16.603715

Todorov B, van de Ven RCG, Kaja S, Broos LAM, Verbeek SJ, Plomp JJ, Ferrari MD, Frants RR, van den Maagdenberg AMJM. 2006. Conditional inactivation of the Cacna1a gene in transgenic mice. *Genesis* **44**:589–594. DOI: https://doi.org/10.1002/dvg.20255, PMID: 17146767

Trotter JH, Hao J, Maxeiner S, Tsetsenis T, Liu Z, Zhuang X, Südhof TC. 2019. Synaptic neurexin-1 assembles into dynamically regulated active zone nanoclusters. *The Journal of Cell Biology* **218**:2677–2698. DOI: https://doi.org/10.1083/jcb.201812076, PMID: 31262725

Wagh DA, Rasse TM, Asan E, Hofbauer A, Schwenkert I, Dürrbeck H, Buchner S, Dabauvalle MC, Schmidt M, Qin G, Wichmann C, Kittel R, Sigrist SJ, Buchner E. 2006. Bruchpilot, a protein with homology to ELKS/CAST, is required for structural integrity and function of synaptic active zones in Drosophila. *Neuron* **49**:833–844. DOI: https://doi.org/10.1016/j.neuron.2006.02.008, PMID: 16543132

Wahl S, Katiyar R, Schmitz F. 2013. A local, periactive zone endocytic machinery at photoreceptor synapses in close vicinity to synaptic ribbons. *The Journal of Neuroscience* **33**:10278–10300. DOI: https://doi.org/10.1523/JNEUROSCI.5048-12.2013, PMID: 23785143

Wang SSH, Held RG, Wong MY, Liu C, Karakhanyan A, Kaeser PS. 2016. Fusion competent synaptic vesicles persist upon active zone disruption and loss of vesicle docking. *Neuron* **91**:777–791. DOI: https://doi.org/10.1016/j.neuron.2016.07.005, PMID: 27537483

Watanabe S, Rost BR, Camacho-Pérez M, Davis MW, Söhl-Kielczynski B, Rosenmund C, Jorgensen EM. 2013. Ultrafast endocytosis at mouse hippocampal synapses. *Nature* **504**:242–247. DOI: https://doi.org/10.1038/nature12809

Watanabe S, Trimbuch T, Camacho-Pérez M, Rost BR, Brokowski B, Söhl-Kielczynski B, Felies A, Davis MW, Rosenmund C, Jorgensen EM. 2014. Clathrin regenerates synaptic vesicles from endosomes. *Nature* **515**:228–233. DOI: https://doi.org/10.1038/nature13846, PMID: 25296249

Watanabe S, Boucrot E. 2017. Fast and ultrafast endocytosis. *Current Opinion in Cell Biology* **47**:64–71. DOI: https://doi.org/10.1016/j.ceb.2017.02.013, PMID: 28391090

Wen W, Turrigiano GG. 2024. Keeping your brain in balance: homeostatic regulation of network function. *Annual Review of Neuroscience* **47**:41–61. DOI: https://doi.org/10.1146/annurev-neuro-092523-110001, PMID: 38382543

Wenk MR, Pellegrini L, Klenchin VA, Di Paolo G, Chang S, Daniell L, Arioka M, Martin TF, De Camilli P. 2001. PIP kinase Igamma is the major PI(4,5)P(2) synthesizing enzyme at the synapse. *Neuron* **32**:79–88. DOI: https://doi.org/10.1016/s0896-6273(01)00456-1, PMID: 11604140

Wilhelm BG, Mandad S, Truckenbrodt S, Kröhnert K, Schäfer C, Rammner B, Koo SJ, Claßen GA, Krauss M, Haucke V, Urlaub H, Rizzoli SO. 2014. Composition of isolated synaptic boutons reveals the amounts of vesicle trafficking proteins. *Science* **344**:1023–1028. DOI: https://doi.org/10.1126/science.1252884, PMID: 24876496

Winther ÅME, Jiao W, Vorontsova O, Rees KA, Koh TW, Sopova E, Schulze KL, Bellen HJ, Shupliakov O. 2013. The dynamin-binding domains of Dap160/intersectin affect bulk membrane retrieval in synapses. *Journal of Cell Science* **126**:1021–1031. DOI: https://doi.org/10.1242/jcs.118968, PMID: 23321638

Winther ÅME, Vorontsova O, Rees KA, Näreoja T, Sopova E, Jiao W, Shupliakov O. 2015. An endocytic scaffolding protein together with synapsin regulates synaptic vesicle clustering in the *Drosophila* neuromuscular junction. *The Journal of Neuroscience* **35**:14756–14770. DOI: https://doi.org/10.1523/JNEUROSCI.1675-15.2015, PMID: 26538647

Wong MY, Liu C, Wang SSH, Roquas ACF, Fowler SC, Kaeser PS. 2018. Liprin-α3 controls vesicle docking and exocytosis at the active zone of hippocampal synapses. *PNAS* **115**:2234–2239. DOI: https://doi.org/10.1073/pnas.1719012115, PMID: 29439199

Zhang JZ, Davletov BA, Südhof TC, Anderson RGW. 1994. Synaptotagmin I is a high affinity receptor for clathrin AP-2: implications for membrane recycling. *Cell* **78**:751–760. DOI: https://doi.org/10.1016/s0092-8674(94)90442-1, PMID: 8087843

Zhen M, Jin Y. 1999. The liprin protein SYD-2 regulates the differentiation of presynaptic termini in *C. elegans*. *Nature* **401**:371–375. DOI: https://doi.org/10.1038/43886, PMID: 10517634

Zürner M, Schoch S. 2009. The mouse and human Liprin-alpha family of scaffolding proteins: genomic organization, expression profiling and regulation by alternative splicing. *Genomics* **93**:243–253. DOI: https://doi.org/10.1016/j.ygeno.2008.10.007, PMID: 19013515